THESIS FOR THE DEGREE OF DOCTOR OF PHILOSOPHY

On the characterisation of steel corrosion and the resulting concrete damage using tomography

Andreas Alhede

CHALMERS
UNIVERSITY OF TECHNOLOGY

Department of Architecture and Civil Engineering
Chalmers University of Technology
Gothenburg, Sweden, 2025

© Andreas Alhede, 2025
All rights reserved. No part of this publication may be reproduced, stored in a retrieval system, or transmitted, in any form or by any means, without prior written permission of the author.

ISBN: 978–91–8103–247–5

Doktorsavhandlingar vid Chalmers tekniska högskola
Technical Report No. 5705
ISSN: 0346–718X

Department of Architecture and Civil Engineering
Chalmers University of Technology
SE-412 96 Gothenburg, Sweden
Phone: +46 (0)31 772 1000
www.chalmers.se

Cover illustration: Cross-sectional image of corroded reinforced concrete obtained via X-ray and neutron computed tomography, showing multimodal data and segmented phases.

Printed by Chalmers Digital Printing
Gothenburg, Sweden, August 2025

There is something inherently compelling about observing concrete reveal its internal structure — an unseen domain, enclosed within the material, yet made accessible through tomography, which enables us to see, measure, and learn from it.

Abstract

Steel corrosion is a major cause of deterioration in reinforced concrete structures. As the process initiates and progresses from within the structure, it remains largely hidden behind the concrete cover, making the assessment of internal damage challenging without invasive or destructive methods. An improved understanding and predictive capability of the internal processes over time is required to improve inspection methods based on observations at the surface. In this research, the internal characteristics of steel corrosion and the mechanisms that lead to damage in reinforced concrete were investigated at the material scale using experimental methods that allow internal processes to be monitored within the specimen.

The overall aim was to characterise steel corrosion and the resulting damage in reinforced concrete at the material scale using X-ray and neutron computed tomography, within the context of accelerated corrosion experiments. The focus was on extracting quantitative information from the tomography data. A subset of the image-derived characteristics were then integrated into a finite element model to gain additional insight into the mechanical effects of corrosion. In addition, other complementary techniques were employed, including distributed optical fibre sensing, electrical resistance measurements and chemical analysis, for monitoring processes that tomography alone could not capture.

The work demonstrated that tomography could be used to quantify a broad range of corrosion and damage-related characteristics. These include the size and spatial distribution of interfacial voids, corrosion penetration depth, corrosion morphology, the volumetric expansion coefficient of corrosion products and the volumetric strain and normal stress in the corrosion layer. Moreover, 3D deformations in the cementitious matrix were measured through local digital volume correlation.

A key finding was the identification of a spatial correlation between larger interfacial voids and pitting corrosion, highlighting void size as a critical factor influencing localised attack. In addition, the volumetric expansion coefficient of corrosion products was found to be close to four, consistent with previous image-based studies. Furthermore, the mechanical response in the corrosion layer indicated a non-linear behaviour of corrosion products. Together, the findings demonstrate how experimental imaging and numerical modelling can be combined to advance the understanding of corrosion-induced damage in reinforced concrete, providing insights that neither approach could provide on its own.

Keywords: Reinforced Concrete, Steel Corrosion, Corrosion-Induced Cracking, Corrosion Characteristics, Tomography, Finite Element Modelling

Sammanfattning

Korrosion av armeringsstål är den främsta orsaken till nedbrytning av armerade betongkonstruktioner. Eftersom korrosionsprocessen initieras och fortskrider inuti konstruktionen, förblir den till stor del dold bakom betongens täckskikt. Därför är det svårt att bedöma inre skador utan att ta till destruktiva metoder. För att kunna utveckla inspektionsmetoder som utgår från observationer av ytan krävs en ökad förståelse för, och förmåga att förutsäga, de inre processer som pågår över tid. Det övergripande syftet var att karakterisera armeringskorrosion och dess mekaniska påverkan i armerad betong, genom experimentella studier på små provkroppar med röntgen- och neutrontomografi inom accelererade korrosionsförsök.

Fokus låg på att kvantifiera parametrar kopplade till korrosion, däribland rostens volymexpansion, fördelning och tjocklek av korrosionlagret, samt tillhörande deformationer såsom sprickmönster och förekomst av luftporer vid armeringsstålet. Ett urval av dessa parametrar integrerades i en finita element-modell för att ge ytterligare insikter om rostens mekaniska egenskaper. Förutom tomografi användes även kompletterande metoder, däribland distribuerad optisk fibermätning, elektriska resistansmätningar och kemisk analys, för att möjliggöra kvantitativa studier av processer som inte kunde studeras med tomografi.

Resultaten visade att tomografi är en kraftfull metod för att kvantitativt analysera ett brett spektrum av parametrar och processer relaterade till korrosion och sprickbildning. Exempel på egenskaper som kunde kvantifieras är storlek och fördelning av luftporer vid armeringsstålet, fördelning av korrosionsdjup längs med och runt om stålet, rostens fria volumetriska expansionskoefficient samt volumetrisk töjning och normalspänning i korrosionslagret. Dörutöver uppmättes tredimensionella deformationer i betongen med hjälp av digital volymkorrelation.

En viktig slutsats var att gropfrätningar ofta uppstod där det fanns luftporer, vilket visar att sådana porer i sig utgör en risk för lokala korrosionsangrepp och att risken ökar med porernas storlek. Vidare konstaterades att den volumetriska expansionskoefficienten för rosten var nära fyra, vilket överensstämmer med tidigare tomografibaserade studier. Den mekaniska responsen i korrosionslagret uppvisade dessutom ett icke-linjärt beteende. Sammantaget visar resultaten hur tomografibaserade experiment och numerisk modellering kan kombineras för att fördjupa förståelsen av korrosionsskador i armerad betong – och därigenom ge insikter som ingen av metoderna kan erbjuda var för sig.

List of Publications

This thesis is based on the following publications:

Paper A

[A] **Andreas Alhede**, Jelke Dijkstra, Samanta Robuschi, Alessandro Tengattini and Karin Lundgren, "A two-stage study of steel corrosion and internal cracking revealed by multimodal tomography". *Construction and Building Materials*, vol. 394, no. 132187, 2023. DOI: 10.1016/j.conbuildmat.2023.132187.

Summary of the paper Modeling of corrosion-induced cracking is limited by lacking knowledge on the behavior of corrosion products. In this work, the corrosion and cracking processes were experimentally investigated in 3D at two different stages. The processes were measured at micro-structural scale, applying nondestructive neutron and X-ray computed tomography in two scans at different stages in the corrosion process. A method to evaluate the average volumetric strain of the compressed corrosion layer was proposed and displacements in the concrete matrix were measured. Strain localization revealed cracks not directly visible in the images. Multimodal tomography demonstrated to be an effective method for investigating steel corrosion in reinforced concrete.

Contribution of the author The author contributed to formulating the research aim, conducted analyses, created figures and was responsible for the planning and writing of the paper.

Paper B

[B] **Andreas Alhede**, Jelke Dijkstra and Karin Lundgren, "Monitoring corrosion-induced concrete cracking adjacent to the steel-concrete interface". *Materials and Structures*, vol. 56, no. 162, 2023. DOI: 10.1617/s11527-023-02252-3.

Summary of the paper Substantial research effort has been devoted on linking corrosion-induced cracking of concrete with the internal corrosion damage level. Still, numerical models of the corrosion and cracking process require internal parameters, that cannot be directly evaluated from experimental data. Therefore, this study provides a novel experimental method for monitoring the effects of steel corrosion adjacent to the steel-concrete interface. This non-destructive method is suited

for small-scale laboratory-made specimen, and was designed to provide missing information required for subsequent calibration of numerical models. Hollow steel bars were cast into concrete and subjected to accelerated corrosion using the impressed current technique. The deformations of the hollow steel bars were measured using distributed strain sensing in an optical fibre, attached to the inner surface of the hollow steel bars. After the corrosion period, X-ray Computed Tomography scans were performed to evaluate concrete cracking and corrosion level. The results reveal a non-uniform distribution of strain around the perimeter of the steel, indicating a non-uniform radial stress distribution. The non-uniformity correlated very well with the position of the corrosion-induced cracks; with extension hoop strains in the steel at the location of these cracks and contraction hoop strains in between. Further, the corrosion level varied around the perimeter, with higher values near cracks. The combination of nondestructive monitoring techniques used in this study on small-scale laboratory-made specimens show great potential to reveal new insights on how the corrosion pattern, corrosion-induced cracking of the concrete cover and stress (indirectly measured through the strain in the steel) interact throughout the corrosion process.

Contribution of the author The author contributed to formulating the research aim, participated in the planning, and was primarily responsible for designing and executing the experimental program. Additionally, the author carried out data analysis, created figures, and wrote the first draft of the paper.

Paper C

[C] **Andreas Alhede**, Jelke Dijkstra, Alessandro Tengattini and Karin Lundgren, "Characterisation of steel corrosion and matrix damage in reinforced mortar combining analytical, electrical and image-based techniques". *Cement and Concrete Research* vol. 190, no. 107792, 2025. DOI: 10.1016/j.cemconres.2025.107792.

Summary of the paper Characterising steel corrosion at the steel-concrete interface and linking it to concrete damage is challenging due to limitations of current non-destructive techniques. This study combines electrical resistance measurements, full-field image-based analyses and analytical techniques to comprehensively characterise steel corrosion and damage in small-scale specimens.

X-ray and Neutron Computed Tomography of two reinforced mortar samples, before and after accelerated corrosion, were used to examine corrosion morphology, interfacial voids, and estimate volumetric strain in the corrosion layer. Inductively Coupled Plasma Mass Spectrometry was employed to measure iron isotope concentrations in water surrounding the specimens.

The results revealed delayed transport of corrosion products relative to mortar cracking. The volumetric expansion coefficients of corrosion products (3.84 and 3.90) align with previous research, and the risk of pitting corrosion correlated with the void size. Overall, the measurements obtained through the various techniques closely aligned with visual observations, providing a robust dataset for calibrating corrosion models.

Contribution of the author The author contributed to formulating the research aim, participated in the planning, and was primarily responsible for designing the experimental program. The author was involved in all experimental work, conducted data analysis, created figures, and wrote the first draft of the paper.

Paper D

[D] **Andreas Alhede**, Jelke Dijkstra and Karin Lundgren, "Linking image-based corrosion characterisation to the mechanical response in reinforced mortar". *Manuscript submitted for publication*, 2025.

Summary of the paper Corrosion of steel reinforcement is a major cause of deterioration in concrete structures, yet the internal stress development associated with corrosion-induced expansion remains poorly understood. Building on recent image-based characterisation of corrosion in reinforced mortar, this study investigates the resulting mechanical response using non-linear finite element analysis. Tomographic data were used to derive spatially varying displacement fields at the steel–mortar interface, applied as boundary conditions to simulate expansion. A parametric study of the stiffness governing interaction between steel and mortar was conducted to evaluate its influence on cracking and internal stress.

The results show that while radial stress was relatively insensitive to these parameters, the time to cracking was strongly affected by the interface stiffness in compression. The relationship between stress and strain in the corrosion layer indicated a non-linear response. This modelling approach provides a mechanistic interpretation of tomography, linking image-derived kinematics to the mechanical response driving corrosion-induced damage.

Contribution of the author The author contributed to formulating the research aim, participated in the planning, and was primarily responsible for constructing the finite element model and conducting all subsequent analyses. The author also analysed the data, compiled the results and wrote the first draft of the paper.

Other publications by the author

Other publications by the author, not included in this thesis, are:

[I] **Andreas Alhede**, Jelke Dijkstra and Karin Lundgren, "X-ray and Neutron Imaging for Steel Corrosion in Concrete: Addressing Challenges and Revealing Opportunities". *12th International Conference on Fracture Mechanics of Concrete and Concrete Structures (FraMCoS 12)*, Vienna, 2025. DOI: 10.21012/FC12.1364.

[II] **Andreas Alhede** and Charlotte Van Steen, "Measuring Corrosion-Induced Deformations in Reinforced Concrete: An Image-Based Approach By Means of X-Ray Computed Tomography". *4th fib International Conference on Concrete Sustainability (ICCS2024)*, pp. 11-18, 2024. DOI: 10.1007/978-3-031-80724-4_2.

[III] **Andreas Alhede**, "Novel approaches for monitoring effects of steel corrosion in reinforced concrete". *Licentiate Thesis. Chalmers University of Technology*, 2023. URL: `https://research.chalmers.se/en/publication/537972`.

[IV] **Andreas Alhede**, Jelke Dijkstra and Karin Lundgren, "Corrosion-induced cracking in reinforced concrete structures: What do we know and how do we move forward?". *XXIV Nordic Concrete Research Symposium*, Stockholm, 2022.

[V] **Andreas Alhede**, Jelke Dijkstra, Samanta Robuschi, Alessandro Tengattini and Karin Lundgren, "Reinforced concrete structures: A nondestructive and noninvasive study of corrosion". *5th International Conference on Tomography of Materials and Structures (ICTMS2022)*, Grenoble, 2022.

Acknowledgments

The work presented in this thesis was carried out between October 2020 and June 2025 at the Department of Architecture and Civil Engineering, Chalmers University of Technology, within the research area of Concrete Structures. The project received financial support from the Swedish Research Council for Sustainable Development (Formas) and the Swedish Transport Administration (Trafikverket).

Several of the experiments relied on image data acquired at the NeXT instrument at the Institut Laue-Langevin (ILL), and at the 4D Imaging Lab at Lund University. I am sincerely grateful to Associate Professor Alessandro Tengattini (ILL and Université Grenoble Alpes) and Professor Stephen Hall (Lund University), whose support and expertise were essential in making these experiments possible.

At Chalmers, the practical and technical support provided by Senior Research Engineers Sebastian Almfeldt and Anders Karlsson played a vital role in the success of much of the experimental work. I am sincerely grateful to you both. I also acknowledge the computing resources provided by Chalmers e-Commons, which supported parts of the data analyses.

I am deeply grateful to my supervisor, Professor Karin Lundgren, and my co-supervisor, Professor Jelke Dijkstra. You have both been exceptional mentors throughout this journey – offering insight and clarity, while also encouraging me to explore, think independently and stay curious. Your support has made this journey both intellectually rewarding and personally meaningful. Throughout these five years of working with you, I often catch myself, on bike rides to and from campus, reflecting on how lucky I have been to truly enjoy this work, a feeling I hope future PhD students will experience too. I hope you continue working together – the synergy of your combined expertise has been a constant source of inspiration!

To all my colleagues at Chalmers, thank you for creating such a friendly and pleasant environment. The many chats, coffee breaks, and shared ideas have contributed more to this journey than you might realise. A special thanks to my office mate and friend, Gabriel Edefors. Having you around has made everyday work more enjoyable, whether through football banter, shared stories or simply a good dose of humour.

Finally, to my parents – thank you for everything. Your unwavering love, encouragement and belief in me have been my foundation throughout this journey. When things were tough, your support carried me through. This thesis is dedicated to you.

Gothenburg, June 2025

Andreas Alhede

Acronyms

CAR:	Corrosion Accommodation Region
DIC:	Digital Image Correlation
DOFS:	Distributed Optical Fibre Sensing
DVC:	Digital Volume Correlation
FEA:	Finite Element Analysis
FFD:	Full Factorial Design
ICP-MS:	Inductively Coupled Plasma Mass Spectrometry
NCT:	Neutron Computed Tomography
ROI:	Region Of Interest
SCI:	Steel-Concrete Interface
SMI:	Steel-Mortar Interface
XCT:	X-ray Computed Tomography

Contents

Part I

Overview

CHAPTER 1

Introduction

1.1 Background

Reinforced concrete rapidly became a widely used construction material in the 19^{th} century due to its increased tensile performance, following Joseph Monier's pioneering work in casting iron into concrete [1]. Today, reinforced concrete is used in numerous applications, including buildings, bridges and other infrastructure. However, as these structures age, they are increasingly prone to deterioration due to repetitive exposure to aggressive environmental conditions.

One of the most critical forms of deterioration is steel corrosion in chloride-rich environments [2], such as coastal areas or regions where de-icing agents are used. Corrosion of steel reinforcement can lead to cracking of the concrete cover, surface discolouration, and eventually the loss of load-bearing capacity [3], [4]. These effects not only increase maintenance demands and expenses [5], [6], but also pose safety concerns if left unaddressed.

A major challenge in assessing corrosion in reinforced concrete structures is the uncertainty regarding both the *location* and the *extent* of corrosion. In most cases, obtaining this information requires the removal of the concrete cover, a destructive, labour-intensive and often costly process [7]. Therefore, to avoid this, researchers have explored the potential of performance indicators, such as crack widths, as

proxies for internal corrosion damage [8]–[16]. While appealing in principle, studies have shown a large scatter in the relationship between surface crack width and steel loss [12], [13], which limits their applicability. The observed scatter likely results from multiple factors that contribute to corrosion damage that vary across tests, including but not limited to differences in corrosion morphology [17], specimen size and geometry [18], material properties (such as strength and porosity) and the degree of confinement [19], [20].

Rather than refining surface-based performance indicators, this thesis takes a closer look at steel corrosion by focusing on the internal characterisation of corrosion and the resulting damage. To support this, existing non-destructive and non-invasive techniques are integrated into an experimental-numerical framework that enables qualitative *observation* of the interior of the specimen and, simultaneously, quantitative *measurement* of key corrosion-related characteristics.

By working at the material scale (mm to cm), using relatively small specimens suitable for imaging, it is possible to acquire detailed tomography data on corrosion characteristics and internal deformations. In future work, these data may be used to calibrate numerical models that are validated through experimental observations, enhancing their accuracy in predicting the corrosion cracking process in reinforced concrete. In the longer term, such models could contribute to the identification of reliable performance indicators that reflect internal corrosion damage, which would be suitable for in-situ assessment supporting targeted and efficient repair work.

1.2 Aim and objectives

The research project was guided by the overarching question: *How and to what extent can contemporary tomography advance the research on steel corrosion in reinforced concrete?* This question formed the basis for the research aim, which focused on using tomographic techniques for both qualitative and quantitative analyses, while also incorporating complementary techniques where necessary.

The aim of the research was to characterise steel corrosion and the resulting damage in reinforced concrete at the material scale, using tomographic techniques. In the present work, *material scale* refers to small-scale specimens with diameters ranging from 26 mm to 88 mm, designed to be suitable for tomography with micro-scale resolution.

To support this aim, four main objectives were formulated:

- **O1:** To design and execute experimental campaigns for monitoring corrosion and cracking in reinforced concrete at the material scale by integrating tomography and other complementary techniques.
- **O2:** To combine, analyse and interpret data from both experiments and finite

element analyses to provide complementary insights into the mechanical effects of steel corrosion in reinforced concrete.

- **O3:** To non-destructively quantify corrosion characteristics and resulting concrete damage.

  In this thesis, the term *corrosion characteristics* refers to measurable physical features of the corrosion process, including, but not limited to, corrosion morphology, penetration depth, volumetric expansion and mechanical response within the corrosion layer (e.g. radial stress and volumetric strain).

- **O4:** To investigate the spatial relationship between interfacial voids, corrosion-induced cracks and corrosion morphology.

1.3 Methodology

A schematic illustration of the methodology adopted is shown in Fig. 1.1. The research started with a comprehensive literature review, focusing on three main areas: (1) corrosion cracking models proposed in the literature, with a focus on their performance relative to experiments and the need for appropriate input data and validation approaches for model calibration, (2) corrosion characteristics, including relevant phenomena and parameters that are essential for calibrating such models, and (3) the application of various non-destructive techniques to quantify these corrosion characteristics. The review provided state-of-the-art knowledge on the topic, supporting the identification of research gaps and the formulation of research objectives.

Four major research studies were conducted. The first involved the analysis of existing X-ray and Neutron Computed Tomography (XCT and NCT) data from a specimen included in a previously completed experiment. This was followed by two experimental campaigns that were designed and executed as part of this PhD project. In these experimental campaigns, XCT and NCT were the main experimental techniques, complemented by other non-destructive methods to obtain data that could not have been acquired through imaging alone. Finally, a numerical study was conducted using finite element modelling, based on experimental data obtained from one of the experimental campaigns.

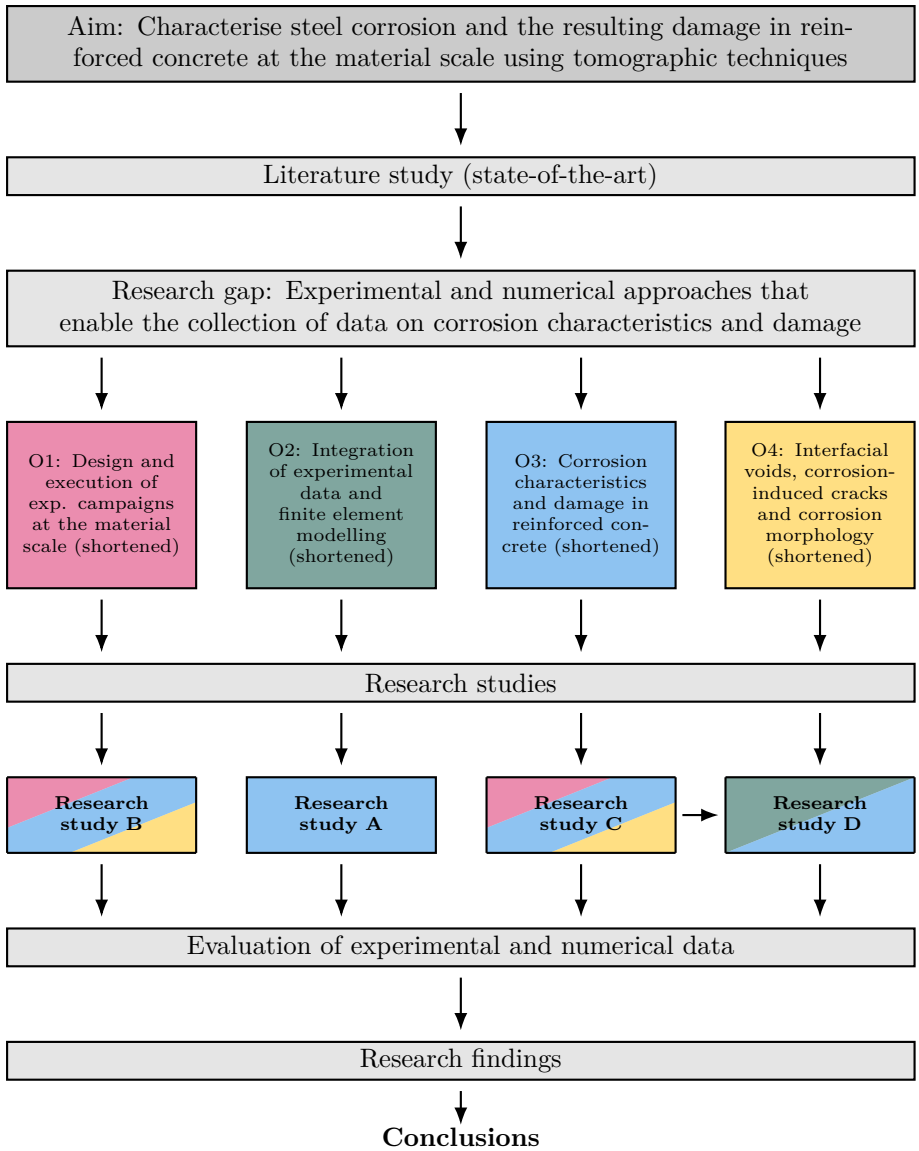

Figure 1.1: Schematic illustration of the methodology followed in the research project.

1.4 Limitations

The main limitation framing this work is that the research is based on a limited number of samples in each experimental campaign. As such, the findings were not statistically verified, which may limit the generalisation of the results.

A number of delimitations were set in the present work. These delimitations apply also to all of the appended papers.

- The research is limited to the material scale only. The geometry and size were specifically designed for imaging applications.
- In all experimental campaigns, steel corrosion was accelerated using an impressed electrical current.
- The research focused primarily on the propagation phase of corrosion. The initiation phase was not studied in detail and was not explicitly considered in the experimental design.
- The focus was on corrosion-induced cracking in reinforced concrete and mortar specimens. Effects of transverse and restraint cracking on the corrosion process were not intentionally studied.

1.5 Original features

The original features of the present work are summarised as follows:

- In **Paper A**, a novel expression for the volumetric strain in the corrosion layer was derived, based on segmented image data obtained from multimodal XCT and NCT.
- In **Papers A and C**, corrosion-induced deformations were measured in 3D using NCT obtained at two different stages in the corrosion process.
- In **Paper B**, experimental measurements of corrosion morphology and concrete cracking were compared with unique measurements of strain in the steel, providing a deeper understanding of the interaction between corrosion morphology, concrete cracking and steel deformations.
- In **Paper C**, the spatially resolved volumetric strain in the corrosion layer was estimated from segmented image data, as a function of both the steel circumference and length. To support this evaluation, electrical resistance measurements and inductively coupled plasma mass spectrometry were used to monitor the cracking process and the transport of corrosion products out of the specimens. This combined information enabled a more informed interpretation of the volumetric strain.

- In **Paper D**, the radial stress in the corrosion layer was estimated using non-linear finite element analysis, where experimental data (**Paper C**) of the normal deformation at the steel-mortar interface, calculated from the evaluated volumetric strain, were prescribed as Dirichlet boundary conditions to simulate the mechanical effects of the corrosion process.

1.6 Outline of thesis

This thesis is composed of an introductory part and four appended papers. The introductory part is organised into five chapters, as described below.

- **Chapter one** introduces the background and motivation for this work. It also presents the research aim, objectives, methodology, limitations and outlines the original contributions of the thesis.
- **Chapter two** provides the theoretical background on which this work is based. It includes an overview of the corrosion process in reinforced concrete, associated structural effects, methods for accelerating corrosion, approaches for on-site assessment and a review of existing research on corrosion characteristics.
- **Chapter three** presents the imaging methodologies used in this thesis, with a focus on XCT and NCT. The chapter describes how these techniques were applied and adapted for the characterisation of corrosion and damage in reinforced concrete.
- **Chapter four** provides a summary of the four appended papers. Each paper is briefly described in terms of its motivation, methods, key findings and their relation to the overall research objectives is discussed.
- **Chapter five** presents the main conclusions of the work and provides suggestions for future research.

CHAPTER 2

Steel corrosion in reinforced concrete

2.1 Electrochemical fundamentals

Corrosion mechanisms

Corrosion of steel reinforcement in concrete is an electrochemical process. Without an external electrical source, such a process requires the simultaneous occurrence of two half-cell reactions: an anodic reaction, in which electrons are released, and a cathodic reaction, in which electrons are consumed [21]. In reinforced concrete, these reactions take place at the Steel-Concrete Interface (SCI), where the anodic reaction involves the oxidation of iron, and the cathodic reaction leads to the formation of hydroxide ions [22]:

$$\text{Anodic reaction:} \qquad \mathrm{Fe} \rightarrow \mathrm{Fe}^{2+} + 2\mathrm{e}^{-} \tag{2.1}$$

$$\text{Cathodic reaction:} \qquad \frac{1}{2}\mathrm{O}_2 + \mathrm{H}_2\mathrm{O} + 2\mathrm{e}^{-} \rightarrow 2\mathrm{OH}^{-} \tag{2.2}$$

These reactions are spatially separated along the reinforcement, requiring two complementary pathways to complete the electrochemical circuit: the flow of electrons from the anodic site through the steel to the cathodic site, and ionic transport in the pore solution to maintain charge balance in the electrolyte. It is evident from the

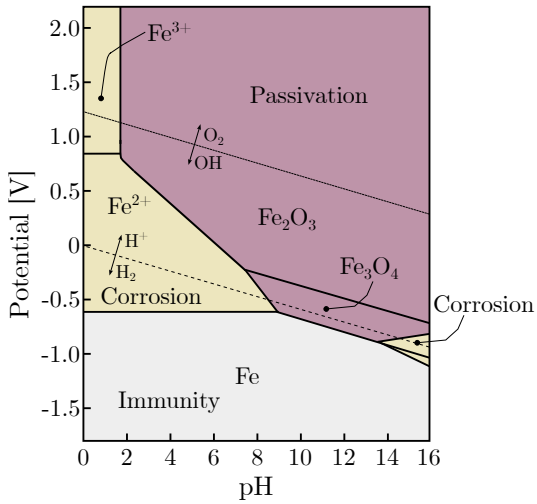

Figure 2.1: Simplified Pourbaix diagram illustrating the electrochemical stability of iron in water at 25 °C, as a function of pH and potential. Adapted from [23].

cathodic reaction that both oxygen and water must be present at the steel surface for corrosion to occur.

The stability of different iron species under various electrochemical conditions can be illustrated using the Pourbaix diagram [23], see Fig. 2.1. This diagram maps regions of thermodynamic stability as a function of pH and electrochemical potential. In the so-called immunity region, iron remains stable and corrosion does not occur. In contrast, the corrosion region represents conditions in which active corrosion is thermodynamically favoured. A third region in the Pourbaix diagram corresponds to passivation, where a thin oxide film forms on the steel surface. This passive layer can significantly reduce corrosion rates, but will deteriorate over time due to a reduction in pH or the presence of chloride ions [24], [25]. In recently cast and chemically intact concrete, the steel reinforcement remains typically in this passivated state.

The corrosion of embedded steel in reinforced concrete is typically initiated by either chloride ingress or carbonation, two distinct mechanisms that can each lead to the breakdown of the passive oxide layer protecting the steel in the high-alkalinity pore solution of the concrete [26]. Once this passive layer is compromised, corrosion may propagate, provided that both oxygen and water are available to sustain the electrochemical reactions.

Carbonation-induced corrosion occurs as carbon dioxide diffuses into the concrete pore system and reacts with calcium hydroxide to form calcium carbonate. This reaction consumes hydroxyl ions, leading to a gradual reduction in pH [25]. The carbonation process initiates at the exposed concrete surface and progresses inward with time, driven by the availability of carbon dioxide and moisture [27]. Once the carbonation front reaches the depth of the embedded steel, the pH of the pore solution may fall below the threshold for passivity, thereby shifting the electrochemical conditions from a passive to an active (corrosive) state.

Unlike chloride-induced corrosion, which often results in highly localised attacks, carbonation-induced corrosion is generally associated with a more uniform corrosion morphology. This is due to the relatively uniform advance of the carbonation front through the concrete cover.

Chloride-induced corrosion occurs when chloride ions, naturally present in seawater and commonly introduced through de-icing agents, diffuse through the cementitious matrix or are transported more rapidly through cracks. If the chloride concentration at the steel surface exceeds a critical threshold, the passive layer degrades, enabling corrosion propagation [24], [28]. Although the threshold concept is widely used for chloride concentration, reported threshold values in the literature vary considerably [29], and the validity of assuming a fixed critical chloride content for depassivation has been questioned [30]. Chloride-induced corrosion is typically localised in nature and often leads to pitting corrosion, which can result in severe steel loss at discrete locations along the steel surface [15].

Corrosion initiation and propagation

Tuutti [26] first introduced a two-phase conceptual model of steel corrosion in reinforced concrete, consisting of an initiation and a propagation phase. According to this model, the initiation phase refers to the period prior to the onset of corrosion, during which aggressive agents such as chlorides and carbon dioxide diffuse into and react with the concrete cover, respectively. The propagation phase begins once the passive layer at the steel surface is locally disrupted and corrosion initiates, leading to the formation of corrosion products and progressive deterioration of both the steel and the surrounding concrete.

The duration of the propagation phase depends on various factors, including the corrosion rate and the degree of structural damage considered acceptable before maintenance is required. The corrosion rate is not necessarily constant over time, it can increase as a result of cracking and spalling of the concrete cover, which facilitate the ingress of oxygen and moisture [31].

Conversely, corrosion products have been observed to accumulate within cracks [32], [33], and it has been suggested that this may reduce the corrosion rate by limiting

the availability of oxygen and moisture at the steel surface [31].

Accelerated corrosion techniques

Accelerated corrosion, also known as artificial corrosion, is widely used in experimental studies of steel corrosion in concrete. It is commonly applied in laboratory experiments to significantly reduce the time required for corrosion-induced damage to develop. Several approaches exist to accelerate corrosion, including the artificial climate environment method, the chloride ion diffusion method and the impressed current technique [34].

The artificial climate environment method accelerates corrosion by mimicking the conditions under which corrosion naturally occurs. It is typically conducted in climate rooms where factors such as temperature, humidity and exposure to saltwater are controlled. Corrosion is facilitated by exposing specimens to repeated wetting–drying cycles in a saline atmosphere, thereby promoting ionic transport similar to that in natural corrosion [35].

The chloride ion diffusion method is used to accelerate chloride ingress by applying an external electric field across the concrete specimen [34]. In this setup, the specimen is placed between two external electrodes in an electrochemical cell, with a saline solution reservoir positioned on the top surface. A voltage applied across the electrodes establishes an electric field that drives chloride ions through the concrete cover toward the reinforcing steel via electromigration [36]. This approach significantly shortens the initiation period by rapidly increasing the chloride concentration at the steel surface, leading to depassivation.

The impressed current technique is based on the principle of electrochemical acceleration. An electrical current is applied between the steel reinforcement, connected to the positive terminal of a power supply and acting as the anode, and a counter electrode, typically made of stainless steel or copper, connected to the negative terminal and acting as the cathode. This configuration promotes anodic dissolution of iron, replicating the electrochemical reactions that occur during corrosion, see Eqs. (2.1)–(2.2).

The applied electrical potential can be adjusted in response to changes in electrical resistance, allowing a constant current to be maintained throughout the experiment. This enables a controlled and predictable corrosion rate, which is important for ensuring reproducibility and allowing consistent comparisons between tests.

To further accelerate the process, the duration of the initiation phase can be significantly shortened by introducing salts, such as sodium chloride, directly into the concrete mix during casting. This results in a high initial chloride concentration at the SCI, which exceeds the threshold for passivity and may inhibit the formation of a stable passive layer.

Compared to natural exposure conditions, the corrosion rates achieved through impressed current can be significantly higher, thereby reducing the duration required to reach a certain level of damage. Corrosion rates under natural conditions are typically reported in the range of $0.1\,\mu A\,cm^{-2}$ to $10\,\mu A\,cm^{-2}$, although more extreme values, up to $100\,\mu A\,cm^{-2}$ have also been observed [10], [37].

While the practical advantages of using impressed current to accelerate corrosion are well established, it remains unclear to what extent this approach replicates the deterioration process observed under natural corrosion conditions. For example, Alonso et al. [10] reported that a greater steel mass loss was required to induce cracking when a current density of $100\,\mu A\,cm^{-2}$ was applied, compared to tests using $10\,\mu A\,cm^{-2}$, the latter being representative for natural corrosion tests. They proposed that the applied current density may influence the type of corrosion products formed, with higher current densities potentially resulting in products with a lower volumetric expansion coefficient. This, in turn, affects the pressure build-up at the SCI and, consequently, the onset of cracking.

In contrast, Hong et al. [38] found that, for the same amount of steel mass loss, cracking occurred earlier when higher current density was applied. They argued that at lower current densities, the slower corrosion rate allowed corrosion products to more effectively diffuse into the surrounding concrete matrix, thereby delaying the build-up of expansive pressure required to initiate cracking. However, this interpretation may not fully capture the complexity of the process, as higher current densities may also enhance ion migration through the pore network and promote electro-osmotic flow [39].

El Maaddawy and Soudki [40] also investigated the effect of impressed current density on corrosion-induced cracking. For comparable levels of steel mass loss, they observed that specimens exposed to higher current densities developed wider cracks. This was attributed to the rapid accumulation of corrosion products at elevated current levels, which they suggested may have limited the diffusion of corrosion products into the surrounding concrete and increased the expansive pressure at the SCI. While the current densities used in their study exceeded those typically associated with natural corrosion, the findings nonetheless suggest that the applied current density can influence the cracking response.

In addition to differences in cracking behaviour, differences in corrosion morphology have also been reported. Ye et al. [41] observed that accelerated corrosion using the impressed current technique tended to produce a more uniform corrosion pattern. In contrast, more localised corrosion was observed in specimens exposed to artificial climate conditions, more closely resembling the morphology found in natural corrosion scenarios.

2.2 Structural effects and assessment methods

Effects of steel corrosion on structural performance

The electrochemical process of steel corrosion has several implications for the structural performance of reinforced concrete. The corrosion products occupy a larger volume than the consumed steel. Because the reinforcing steel is embedded within the concrete, the volumetric expansion of corrosion products is restrained. Consequently, splitting stresses are induced at the SCI which may lead to cracking of the concrete cover. If such cracking occurs on the compressive side of the cross-section, it can reduce the effective compressive zone, thereby reducing the ultimate load-carrying capacity of the section [42].

Corrosion of steel reinforcement leads to a progressive separation between the steel and the surrounding concrete at the interface. The evolution of bond deterioration depends on factors such as the degree of confinement (e.g. the presence of transverse reinforcement) and the type of bar (e.g. ribbed or plain). In confined conditions, early-stage corrosion can enhance bond strength due to the corrosion-induced expansion, which increases the friction up to the point at which cracking initiates. At higher corrosion levels, the bond strength may remain relatively stable, likely because the transverse reinforcement restrains the cross-section, thereby preserving the mechanical interaction necessary for effective stress transfer from the steel to the concrete [43].

In contrast, under unconfined conditions and for plain bars, minor corrosion can increase the bond strength by roughening the steel surface and enhancing the frictional resistance [44]. Moreover, the position of the reinforcement within the cross-section, whether top- or bottom-cast, also influences the bond behaviour. Top-cast bars, typically surrounded by less dense concrete, have been shown to exhibit an initial increase in bond strength due to greater corrosion accommodation before cracking occurs. Bottom-cast bars, in contrast, experience earlier concrete cracking and more pronounced bond degradation [45].

As corrosion progresses and cracking initiates, the bond strength deteriorates significantly, primarily due to the loss of confining stresses that reduce friction. Additional losses arise from the breakdown of adhesion and, in the case of ribbed bars, the degradation of mechanical interlock. As a result, corrosion may critically impair the capacity for stress transfer in anchorage regions [43].

If the experimental investigation of bond degradation is based on accelerated corrosion, the applied current density has been shown to influence both crack development and corrosion morphology, often resulting in an overestimation of bond loss compared to naturally corroded structures [46]. This underlines the importance of keeping such methodological differences in mind when comparing experimental

results or interpreting their relevance for engineering structures.

Beyond damage to the concrete and bond deterioration, corrosion also reduces the effective steel cross-section, thereby further decreasing the ultimate capacity of the reinforced concrete section. In the case of pitting corrosion, this loss can be significant, leading to local stress concentrations within these regions [47]. These stress concentrations, in turn, reduces the fatigue performance of the reinforcement, increasing the risk of premature failure under cyclic loading [48], [49].

Lastly, the reduction in steel cross-sectional area leads to a decrease in both the ultimate steel strain and the ratio of ultimate to yield stress, thereby reducing the ductility of the reinforcement [50], [51]. This loss of ductility compromises the ability of the structure to undergo large plastic deformations before failure, an aspect of particular concern as current design codes typically require a minimum ductility to ensure a sufficient rotational capacity [52], [53] and to comply with seismic design [50].

Assessment techniques for corrosion-induced damage

A wide range of techniques has been employed to assess corrosion in reinforced concrete structures. These can broadly be classified into non-destructive and destructive methods. This section focuses on commonly used non-destructive techniques, grouped by the type of information they provide. Although numerous techniques exist, the focus here is on representative examples that illustrate the range of measurable parameters and practical limitations involved in corrosion assessment.

Visual inspection

Visual inspection is the most widely used approach for assessing the structural condition of a structure. It enables the identification of visible indicators, such as rust stains, cracking and spalling, which may suggest underlying deterioration [3]. These surface observations are used to determine whether more detailed investigation is necessary. It is important, however, to recognise that the absence of visible surface indicators does not necessarily imply the absence of ongoing corrosion. Corrosion may progress undetected for extended periods, particularly in the case of localised corrosion such as pitting. As previously noted, this local mechanism can lead to significant reductions in the cross-sectional area of embedded steel without producing visible traces on the concrete surface [54]. The limitations of visual inspection have been highlighted not only in reinforced concrete structures but also in post-tensioned systems, where the inaccessibility of tendons has, in several documented cases, resulted in unexpected failures despite the absence of observable warning signs [55]. While visual inspection remains a valuable first step in condition assessment, these

cases underscores the risk of relying solely on surface-based indicators.

Polarisation resistance

The polarisation resistance method is an electrochemical technique that enables on-site assessment of the corrosion current density in reinforced concrete structures. It involves applying small shifts in electrochemical potential relative to the resting potential of the steel, and measuring the resulting corresponding current response at each step. The slope of the voltage-current relationship, referred to as the polarisation resistance, is inversely proportional to the corrosion current density. To calculate the corrosion current density, the measured current is normalised by the surface area assumed to be polarised [56], [57].

However, several limitations must be considered when interpreting the results. Because the actively corroding area is typically unknown, the method is generally more suitable to corrosion driven by carbonation, which tends to produce a more uniform corrosion morphology along the reinforcement. In contrast, chloride-induced corrosion often leads to localised attack; therefore, if the actual corroding area is much smaller than assumed, the corrosion current density may be significantly underestimated. This limitation is particularly relevant when assessing the extent of corrosion, as pitting corrosion can lead to severe cross-sectional loss without influencing the average current over the assumed polarised area. To account for this, a conservative "pitting factor" is sometimes applied to adjust the estimated corrosion rate [56].

Accurately defining the polarised area also remains a challenge in on-site applications, particularly in the absence of a guard ring to confine the current flow. In addition, environmental factors such as moisture content and temperature affect the electrical resistivity of the concrete, which in turn influences the polarisation measurements [57]. For these reasons, the method requires careful interpretation and is best applied through repeated measurements under varying environmental conditions to obtain a representative estimate of the corrosion activity.

Half-cell potential

Another electrochemical technique for assessing corrosion activity is the half-cell potential method. It involves connecting the steel reinforcement to a high-impedance voltmeter and measuring its electrical potential relative to a reference electrode placed on the concrete surface. This measured potential, the "corrosion potential", provides an indication of the likelihood of ongoing steel corrosion, where more negative values are associated with a higher probability of corrosion [58].

The half-cell potential method can be used to generate potential maps, enabling spatial identification of anodic and cathodic regions. This facilitates the detection

of high-risk areas and supports decisions regarding further testing or maintenance. Moreover, the method can be repeated over time to monitor changes in corrosion activity.

However, the method does not provide a direct measurement of the corrosion current density which makes it difficult to assess the severity or extent of corrosion damage. Furthermore, the spatial resolution of the potential mapping is limited by the electrode spacing; if the spacing is too large, local regions with pitting may remain undetected. The results are also influenced by factors such as moisture content, chloride contamination, temperature and concrete cover thickness, all of which affect electrical resistivity of the concrete and, consequently, the measured potential [58], [59].

Acoustic emission

While electrochemical techniques are used to assess the likelihood and rate of ongoing corrosion processes, they do not provide information on the mechanical effects caused by corrosion, such as cracking. In this context, acoustic emission monitoring offers a complementary approach by detecting the structural response to corrosion, particularly the formation and propagation of cracks.

When a discontinuity, such as a crack, forms or propagates, a portion of energy is released as transient elastic waves. These high-frequency stress waves travel through the concrete and are detected by acoustic sensors, which are mounted on the concrete surface. The source of emission events can be localised in one, two or three spatial dimensions depending on the number and placement of sensors. The dimensionality of the setup determines the level of spatial information that can be retrieved, from axial location to full spatial mapping [60].

A main advantage in acoustic emission lies in the ability to capture damage-related processes in real time, making it suitable for local and global structural health monitoring. In corrosion-related applications, acoustic emission can identify the onset of cracking due to steel corrosion and has been used to monitor, for example, the fracture of corroded tendons in prestressed concrete and debonding damage [44], [61]–[63].

Despite these advantages, several challenges remain for routine use in the assessment of built infrastructure. The signals of acoustic emission attenuate significantly in concrete, especially at higher frequencies, limiting the localisation accuracy for deep or distant sources. In addition, structures in service are often exposed to various forms of environmental and operational noise, such as wind-induced vibrations or traffic loads, which complicates the interpretation of the recorded data. Advanced filtering techniques and continuous signal classification are therefore required to distinguish relevant damage-related emissions from background activity [60], [64].

2.3 Characteristics relevant for modelling of corrosion-induced cracking

While numerous modelling approaches, such as analytical (see for example [65]–[67]), and numerical (see for example [68]–[70]) have been developed to simulate the corrosion-induced cracking process in reinforced concrete, the accuracy and applicability ultimately depend on the availability of reliable input parameters. Yet, several fundamental material and interface properties that govern corrosion-induced damage remain insufficiently understood or idealised in modelling efforts.

Volumetric expansion coefficient of corrosion products

As noted in Section 2.2, corrosion products occupy a greater volume than the steel from which they form. This increase in volume depends on the type of corrosion product and is typically reported as a volumetric expansion coefficient ranging from approximately two to six times the volume of the consumed steel [26]. This parameter is therefore an essential parameter in modelling of the corrosion-induced cracking process as it influences the development of splitting stresses generated at the SCI.

Despite its central role in modelling, the volumetric expansion coefficient remains difficult to quantify reliably and is therefore often assumed. This uncertainty arises from the complex and evolving nature of corrosion products, whose characteristics are strongly influenced by electrochemical and environmental conditions. For instance, the oxygen availability affects the phase formation: compact products tend to form under oxygen-limited conditions, whereas more porous and expansive phases are typical in oxygen-rich environments [71]. The presence of chlorides or carbonates further influences the types of corrosion products that form [31], while steel properties, such as microstructure and surface condition, may also influence the composition and morphology of the resulting corrosion layer[72].

Consequently, the volumetric expansion coefficient is not only highly dependent on exposure conditions but may also vary temporally, as cracking or changes in moisture and oxygen availability alter the local environment at the SCI. This temporal and environmental variability further complicates a reliable quantification. A discussion on the experimentally obtained volumetric expansion coefficients in this thesis, including their comparison with values reported in the literature, is provided in Section 4.3.

Mechanical behaviour of corrosion products

The mechanical behaviour of corrosion products in reinforced concrete is an essential parameter in modelling of the corrosion-induced cracking process. Since stress-free

expansion at the SCI is constrained by the surrounding concrete, the stiffness of the corrosion products influences the magnitude of splitting stresses that develop. A stiffer corrosion layer transfers a greater portion of the expansion-induced deformation to the concrete, thereby generating higher internal stresses. Conversely, a more compliant corrosion layer accommodates a larger share of the deformation internally, resulting in lower stresses in the concrete. As such, the stiffness of the corrosion layer significantly affects the onset and progression of cracking in the surrounding concrete.

Various studies have attempted to quantify the stiffness of corrosion products, often reporting Young's modulus values based on micro- or nanoindentation measurements. However, the reported values differ significantly, from less than 1 MPa to over 160 GPa [73], [74]. This wide scatter likely reflects a combination of factors, including inaccuracies in the composition and phase of the corrosion products, effects of confinement (i.e., whether the corrosion products have previously been mechanically loaded) and measurement artefacts. In nanoindentation, for example, errors in estimating the contact area or identifying the point of initial contact between the indenter and the sample can lead to significant inaccuracies in the calculated modulus [75].

Some studies have focused on characterising the bulk mechanical response of corrosion products, reporting their stress-strain behaviour. Ouglova et al. [76] and Xu et al. [77] conducted confined uniaxial compression tests on dried corrosion products. In both cases, the stress-strain response was highly non-linear at low stress levels, likely due to initial compaction of the porous corrosion products, which exhibit both intergranular voids between particles and intragranular porosity within the grain themselves. As the applied stress increased, the response gradually stiffened, showing a transition toward a quasi-linear regime.

Zhao et al. [73] investigated the response under unconfined conditions using cyclic loading and unloading. They reported a strongly non-linear response during the first loading cycle, while subsequent cycles exhibited a nearly linear response, suggesting irreversible compaction effects. In a complementary approach, Lundgren [68] used experimental observations in combination with Finite Element Analysis (FEA) to describe a non-linear constitutive stress-strain relationship.

Fig. 2.2 summarises reported stress-strain responses compiled from the literature. While the experimental setups and methods differ among the studies, the figure is intended to illustrate the wide variation in mechanical behaviour rather than enable direct quantitative comparison. However, despite differences in test conditions and material states, the reported stress–strain responses consistently indicate a non-linear mechanical behaviour of corrosion products.

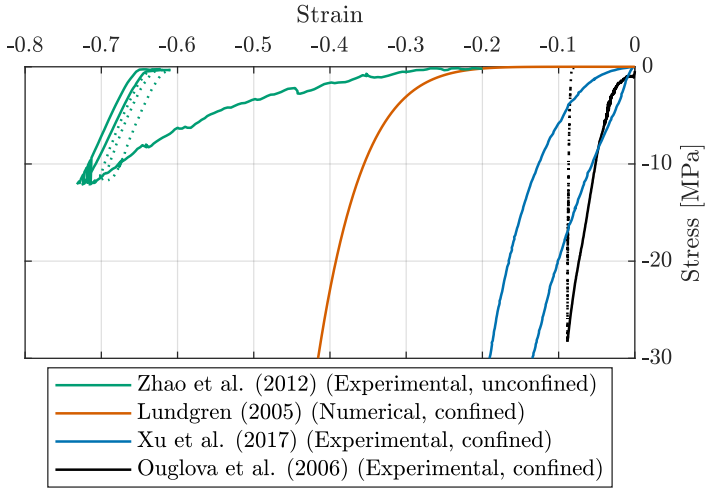

Figure 2.2: Stress-strain relationships for corrosion products as reported in literature. Solid lines represent loading and dotted lines unloading. Data compiled from Zhao et al. [73], Lundgren [68], Xu et al. [77] and Ouglova et al. [76].

Corrosion accommodating region

The idea of a zone at the SCI that temporarily accommodates corrosion products was introduced in modelling efforts to better reproduce the observed initiation of corrosion-induced cracking. Liu and Weyers [66] proposed a "porous zone" where corrosion products could initially accumulate without inducing expensive pressure, thereby delaying the onset of cracking. Later modelling efforts showed that incorporating such a parameter improved agreement between models and experimental results [78].

Although the physical existence of such a zone has been questioned [79], the concept remains compelling from a mechanistic perspective. A useful analogy can be drawn with the interfacial transition zone between aggregate particles and cement paste, where a region of higher porosity is known to form. This is attributed to the inability of dry cement particles to pack densely against the relatively large aggregate surface during mixing, resulting in a locally higher porosity compared to the bulk hydrated cement paste [80].

Now often termed the Corrosion Accommodating Region (CAR) [81], its reported thickness varies widely – from 0.002 µm [82] to over 100 µm [67], [83]. There are likely

several reasons for this scatter. First, the composition of the concrete, particularly the water-to-cement ratio, affects the porosity of the cement paste and may therefore influence the potential size of the CAR. Second, the experimental resolution required to accurately detect and quantify such a narrow interfacial zone is high, and many studies are limited by the techniques employed. Accurately resolving the presence and the extent of the CAR requires high spatial resolutions, and many studies may be limited by the resolution of the techniques employed, particularly imaging. As such, both variability in material compositions and methodological limitation plausibly contribute to the wide range of reported values in the literature.

2.4 Review of image-based studies on steel corrosion

This section presents a literature review of previous studies that have investigated steel corrosion in reinforced concrete using X-ray and neutron imaging. The reviewed studies are grouped according to the phenomena observed. The underlying principles of these imaging techniques, along with their analytical capabilities, are described in detail in Section 3.1.

Beck et al. [84] were among the first to explore the application of X-ray Computed Tomography (XCT) for studying steel corrosion in reinforced concrete. Since then, both radiography and tomography have been increasingly employed for both qualitative *observations* of the corrosion and cracking processes and for quantitative *measurements* related to the characterisation of steel corrosion and the resulting damage in concrete.

One of the earlier studies, by Michel et al. [81], employed 2D X-ray radiography to monitor the progression of steel corrosion and corrosion-induced cracking in reinforced mortar. Corrosion products were observed to form at discrete regions of the steel, gradually spreading over a larger portion of the bar with time. The process was characterised by a high degree of spatial variability, both in the rate of corrosion formation and in the development of radial expansion.

In a related effort, Šavija et al. [85] employed sequential XCT to monitor the progression of steel corrosion over time, reporting localised thickening of the corrosion layer in regions adjacent to interfacial voids and cracks. Other studies have similarly investigated spatial correlations between corrosion products and concrete damage. For example, Zhang et al. [86] used Neutron Computed Tomography (NCT), to visualise corrosion products, which were predominately concentrated in regions of cracking. This accumulation is likely due to locally enhanced access to water and oxygen, whose availability, as discussed in previous sections, may differ from that at the SCI.

Beyond general observations of corrosion and cracking, several studies have specifically addressed the role of interfacial voids in corrosion initiation. Rossi et al. [87] investigated chloride-induced corrosion in twenty-year-old reinforced concrete specimens using XCT. They found that pitting corrosion occurred in or adjacent to nearly all interfacial voids, suggesting that these voids, and their internal environment, may act as hot-spots for corrosion initiation.

The role of interfacial voids was also examined by Angst et al. [88], who analysed specimens from a fifteen-year-old bridge using multimodal XCT and NCT. While more than 90 % of the interfacial voids remained free from corrosion, approximately 50 % of the corrosion spots were located in or near such voids. This suggests that although interfacial voids may not independently trigger corrosion, their presence is likely not coincidental and may contribute to corrosion formation under specific conditions. Factors such as the saturation state of interfacial voids and the local moisture content at the SCI were proposed as possible explanations for the observed variability, highlighting the complex and condition-dependent role of interfacial voids in corrosion processes.

Other studies have utilised the capabilities of multimodal imaging techniques to quantify parameters relevant for modelling. Robuschi et al. [89] combined XCT and NCT to investigate steel corrosion in two specimens: one exposed to natural corrosion and one to accelerated corrosion. In the naturally corroded specimen, no visible cracking was observed at the time of imaging, which limited the ability to assess how corrosion products migrated through the sample. In the accelerated corroded specimen, however, corrosion products were found to migrate predominantly along larger cracks. In addition to qualitatively investigating transport of corrosion products, the study also quantified steel loss, the thickness of the corrosion layers and interfacial voids. The free volumetric expansion coefficient of corrosion products was also estimated by relating the volume of steel loss to the volume of corrosion products partially filling interfacial voids.

Further insights into the link between corrosion products and cracking were provided by Michel et al. [90], who investigated how corrosion products penetrate into the surrounding cementitious matrix and contribute to cracking. Using X-ray attenuation measurements and Digital Image Correlation (DIC), they observed that the development of expansion-induced stresses in the cementitious matrix was delayed relative to the initial formation of corrosion products. The corrosion products were found to accumulate in the CAR, and as long as this region remained unfilled, the products expanded without exerting significant pressure on the surrounding matrix. Crack initiation was detected using DIC, which enabled the authors to estimate the timing of mechanical response in the cover relative to the formation of corrosion products.

CHAPTER 3

X-ray and neutron computed tomography

A main experimental method enabling this work is the combination of X-ray Computed Tomography (XCT) and Neutron Computed Tomography (NCT) applied to specimens at the material scale.

3.1 Imaging principles

Both XCT and NCT provide a 3D image of the investigated sample, revealing the internal structure of the sample without the need for destructive sample preparation. Their differing contrast mechanisms, i.e. the variations in material properties they are sensitive to, make the techniques highly complementary. While X-rays interact primarily with the electron shells of atoms, neutrons interact with the atomic nuclei [91]. As a result, XCT is particularly effective for imaging materials with high X-ray attenuation, such as concrete and steel, whereas NCT is more sensitive to light elements, including hydrogen, making it suitable for identifying hydrogen-rich phases such as cement paste and corrosion products.

The two modalities provide fundamentally different attenuation fields due to the nature of their interactions. In both cases, attenuation is often assumed to follow the Beer-Lambert law, which relates the intensity of the transmitted beam, I, to the

incident intensity, I_0 for a homogeneous material of constant thickness l [92]:

$$I = I_0 e^{-\mu l} \tag{3.1}$$

here, μ is the linear attenuation coefficient, a material property reflecting the interaction of the beam with the sample. For X-rays, μ depends on the atomic number of the material and beam energy [93]. For neutrons, it is primarily influenced by the isotope composition and the energy of the neutron beam [94].

A 3D image stack is reconstructed from a series of 2D vertical projections captured as the sample is rotated along its longitudinal axis. For each projection, a detector measures the transmitted beam intensity relative to the incident beam intensity, capturing attenuation information at different angular positions and thereby contributing unique data about the internal structure of the sample. The intensity data record is subsequently converted into greyscale values representing the attenuation of the material, where a higher attenuation results in brighter pixels and lower attenuation in darker pixels. These projections are then reconstructed into a 3D volume, with the Filtered Back Projection algorithm being a commonly used method [95].

The quality of the reconstructed image depends strongly on the angular sampling density. Jacobsen [96] showed that undersampling in the angular domain can result in streaking artefacts and reduced spatial resolution in the tomographic reconstruction. These effects are particularly unfavourable in the present work, where accurate resolution of fine features such as corrosion products and cracks is essential. For reference, the Nyquist sampling criterion for parallel-beam geometries suggest that the number of projections should be at least π times the number of detector pixels spanning the diameter of the sample [97]. In this thesis, the number of projections was approximately 1.6 times the number of voxels spanning the sample diameter, reflecting the use of cone-beam geometry in XCT.

Beyond angular sampling, the quality of each projection was improved by averaging multiple frames [98]. This approach improved the signal-to-noise ratio and subsequently improved the quality of the reconstructed datasets.

Fig. 3.1 shows a horizontal slice of a reinforced concrete sample, with data acquired from both XCT (left) and NCT (right), along with their corresponding probability distributions of greyscale values. As shown in the figure, steel, concrete and voids are clearly identified from the XCT, while cement paste and aggregates are clearly distinguishable from the NCT.

The smallest unit in a reconstructed image is the voxel, the 3D equivalent of a pixel. In cone-beam XCT systems, voxel size is determined by the detector pixel size and the geometrical magnification, which is defined as the ratio between the source-detector distance and the source-object distance [99]. Hence, larger specimens, which

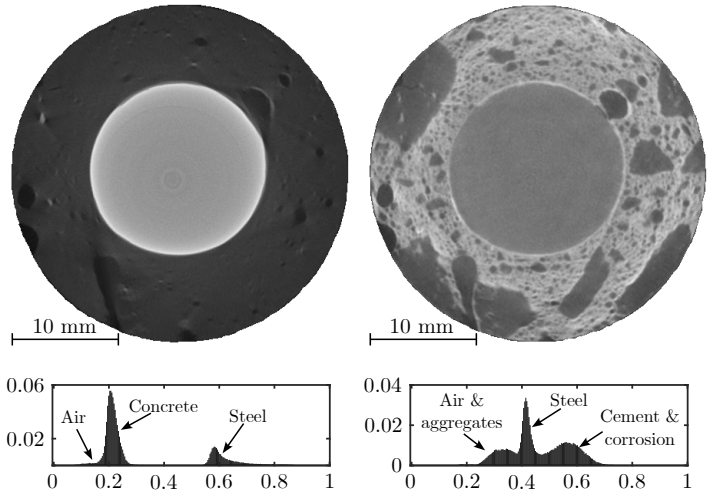

Figure 3.1: A horizontal slice of a reinforced concrete sample with data acquired from XCT (left) and NCT (right) along with their corresponding normalised greyscale histogram.

cannot be placed close to the X-ray source, yield coarser voxel sizes. The need to capture the entire specimen within the field of view imposes further constraints on achievable resolution.

In neutron imaging, the beam is shaped by directing neutrons through a small aperture (pinhole), producing a cone-shaped beam. The degree of beam collimation is described by the L/D ratio, where L is the distance from the pinhole to the centre of the sample, and D is the diameter of the pinhole [100]. A higher L/D ratio results in improved spatial resolution (i.e. smaller voxel size), but at the expense of reduced neutron intensity (flux) and consequently longer exposure times are required to maintain signal to noise. Conversely, a lower L/D ratio increases neutron flux but reduces spatial resolution. In this thesis, the L/D ratio and the exposure time were selected to balance achievable resolution with practical scan durations (typically on the order of hours) depending on the sample geometry and experimental constraints, such as degree of saturation.

While voxel size defines the smallest unit of volume in the reconstructed image, it does not by itself determine what physical property it represents. Accurate interpretation relies on evaluating the spatial variation in greyscale values across adjacent voxels, which provides the contrast needed to identify fine features in the image. This capability is governed by the image *resolution*, which reflects the ability to dis-

tinguish closely spaced details. Since resolving such fine features typically requires differences in intensity values over multiple voxels, resolution is generally lower than the nominal voxel size.

To reduce imaging artefacts, i.e. features in the image that were not originally in the specimen and are created by the imaging technique, several strategies were applied both prior to scanning and after image reconstruction. One key artefact in XCT is beam hardening, which originates from the polychromatic nature of laboratory X-ray sources. As the beam passes through the sample, lower-energy X-rays are absorbed more strongly than higher-energy ones. This produces the beam to progressively "harden", meaning that the average energy increases with depth, resulting in a non-linear attenuation response that depends on both material composition and path length [93]. Within the current application, beam hardening artefacts caused the steel to appear artificially brighter near its boundaries due to elevated local attenuation close to the steel-concrete interface (SCI), see Fig. 3.1. Similar artefacts were also observed at the boundaries between concrete and voids.

While certain strategies help reduce beam hardening artefacts, it is difficult to eliminate them entirely, particularly when the sample contains high X-ray attenuation materials such as steel. One common approach is to place thin metal sheets (e.g. copper and iron) in front of the X-ray source [101]. These filters absorb the low-energy portion of the X-ray spectrum, thereby increasing the average energy of the beam and reducing the image artefacts.

Another way to reduce beam hardening is to increase the potential (kV) and current (µA) of the X-ray source, which shifts the energy spectrum toward higher photon energies. However, this approach is constrained in laboratory XCT systems, where the maximum acceleration voltage is typically limited.

Despite these mitigation efforts, some beam hardening remained visible in the XCT. To correct this, a post-processing procedure based on Stamati et al. [102] was applied. The procedure assumes that beam hardening induces a radial greyscale bias that varies with distance from the specimen centre. To estimate this artefactual intensity profile, radial grey value trends were fitted separately for two reference phases: voids (low attenuation) and aggregates (high attenuation). These fitted trends were then used to normalise the grey values across the image using a linear transformation. As a result, the greyscale gradient within the concrete matrix was flattened, and the greyscale values of individual phases became more uniform. This enhanced the robustness of the segmentation process, particularly near boundaries between concrete and voids, by reducing the sensitivity to radial artefacts caused by beam hardening.

Multimodal imaging

Segmentation is the process of dividing a continuous greyscale image into distinct groups based on their greyscale values. The goal is to identify and classify regions of the image according to the material phases they represent [103]. Although XCT and NCT individually provide valuable insights, each modality has limitations.

In NCT, it is difficult to differentiate between aggregates and voids, as their attenuation coefficients are similar. In contrast, XCT provides strong contrast between these phases, making voids clearly distinguishable. Similarly, corrosion products and cement paste exhibit comparable attenuation in NCT, which complicates their segmentation. This challenge is further exacerbated at high moisture content in the specimen, where the strong neutron attenuation by hydrogen increases image noise, making it even harder to distinguish corrosion products from cement paste. At lower degree of saturation, however, segmentation of corrosion becomes more feasible. In XCT, corrosion products attenuate X-rays more than the concrete but less than the steel. However, residual beam hardening artefacts can still complicate their precise segmentation. On the other hand, the attenuation of neutrons by cement paste and aggregates differs strongly, allowing these two phases to be clearly distinguished.

The integrated use of both modalities enables a more comprehensive analysis by exploiting their complementary contrast mechanisms. This is achieved through a multimodal imaging approach, which takes advantage of the mutual information between datasets acquired of the same sample [104]. By registering (aligning) the XCT and NCT in space, their greyscale values at corresponding voxel positions can be analysed jointly. This registration process, described in detail in the following section, involved aligning the image data acquired in different frames and at different resolutions [105]. Careful registration is essential to ensure that the corresponding material features are correctly matched across modalities.

A useful way to visualise the relationship between XCT and NCT greyscale values is through a 2D (joint) histogram, where each axis represents greyscale intensities from one modality, and their co-occurrence frequency is plotted as a density distribution. This histogram provides insights into material contrast across modalities, revealing correlations that assist in image segmentation by linking specific greyscale combinations to distinct material phases.

As shown in Fig. 3.2, the joint histogram for the horizontal slice of a reinforced concrete sample (the same as illustrated in Fig. 3.1) displays three dense clusters, corresponding to steel, aggregates and cement paste. The attenuation characteristics of these materials appear relatively uniform, suggesting a strong correlation between the two modalities. There is also a scattered region, associated to voids, which show low attenuation in both XCT and NCT. The variability in these regions suggests that not all voids exhibit identical attenuation, likely due to the presence of water

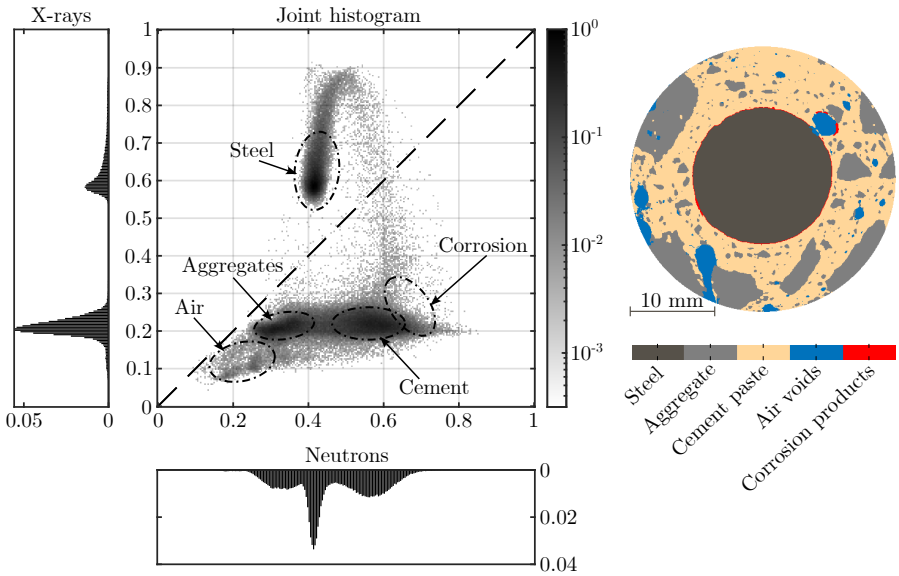

Figure 3.2: Joint histogram (left) illustrating the correlation between XCT and NCT greyscale values, with denser regions corresponding to distinct material phases. The segmented image (right) shows the classification of steel, aggregates, cement paste, air voids and corrosion products based on the histogram.

or corrosion products, which modifies local attenuation. Furthermore, a distinct region corresponds to corrosion products, which have greyscale values similar to cement paste in NCT but become more distinguished when considering their joint attenuation. Lastly, some noise representing data points with low correlation is present. This can primarily be attributed to minor misalignments between the datasets, arising from registration, and to image noise [106]. Therefore, sub-voxel registration accuracy is important to improve segmentation quality.

Local digital volume correlation

Digital Image Correlation (DIC) is a 2D technique for measuring full-field (entire field of view) displacement fields on a surface [107]. The fundamental principle of DIC is to track greyscale patterns within images taken before and after deformation, enabling the measurement of in-plane displacement and strain fields. However, because conventional camera-based images only capture surface information, internal

deformations remains inaccessible. Digital Volume Correlation (DVC) applies the same underlying correlation algorithm as in DIC, but extends it into 3D, allowing for the measurement of internal displacement and strain fields by analysing tomographic data [108], such as XCT and NCT.

There are two common approaches to DVC: local and global. In the local approach, the volume is divided into smaller subvolumes, *subsets*, and displacements are measured using subset-based correlation between the undeformed and deformed configurations. This approach does not impose continuity constraints, meaning that the displacement computed for one subset does not affect or depend on the displacement of adjacent subsets. A simplified 2D schematic of the local DVC is shown in Fig. 3.3. In contrast, the global approach determines displacement fields using a global representation that enforces continuity across the volume [109]. This method is often referred to as the finite element-based DVC, as it uses a finite element mesh to describe the displacement field. While studies have reported conflicting results regarding the accuracy of the local versus global DVC [108], [109], the local approach is more commonly used due to its computational efficiency and its ability to handle displacement discontinuities [110], [111].

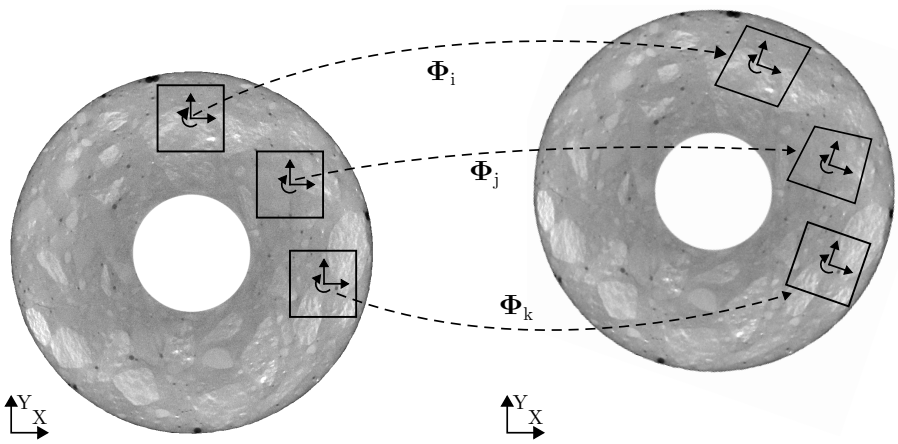

Figure 3.3: A simplified 2D illustration of the local DVC. The volume is divided into subsets, and displacements are measured by computing a field of transformations $\mathbf{\Phi}$. The left-hand image shows the reference (undeformed) configuration, and the right-hand image shows the deformed configuration. Subsets are highlighted in both images, with an arrow indicating the transformation $\mathbf{\Phi}$ that maps the subset from the reference to the deformed state.

Given these considerations, the local DVC approach was adopted for all DVC analyses in the appended papers. As described earlier, the local approach is subset-based, meaning that the volume is divided into smaller subsets. Each subset contains a unique pattern of greyscale values, which serves as a reference for measuring displacement between the undeformed and deformed states. For each subset, a transformation gradient tensor $\mathbf{\Phi}$ is computed to describe the optimal mapping between the undeformed and deformed states. This tensor accounts for translation, rotation, scaling and shear and is computed at a node located at the centre of gravity of each subset.

DVC is inherently an ill-posed problem, as multiple displacement fields may satisfy the correlation residuals, defined as the difference in greyscale intensity between the deformed configuration and the warped undeformed configuration at each voxel, leading to non-unique solutions. To mitigate this issue, least squares optimisation is commonly applied, minimising the sum of squared residuals between the reference and deformed images. The algorithm iteratively updates the displacement field and the convergence is assessed by checking whether the sum of squared residuals falls below a predefined error tolerance. If the sum of squared residuals does not meet the tolerance, additional iterations are performed, often using the Newton-Raphson method to update the transformation gradient tensor until convergence is achieved. For further details on the local DVC script used, see [112].

Several complexities can arise when performing a DVC analysis, but these can be handled effectively by following an appropriate workflow. The local DVC procedure was iterative, and the approach adopted in this study is outlined below and in Fig. 3.5.

1. **Image registration:** Image stacks acquired at different time intervals may not be perfectly aligned due to positional offsets, sample rotations and differences in resolution between the two scans. To correct for these misalignments, an image registration was performed, aligning the entire sample volume to the deformed configuration. This step yields a single transformation gradient tensor that describes the best-fit global mapping between the datasets. The resulting transformation was used as the initial estimate for the local DVC. An accurate image registration is *essential*, as it ensures that the datasets are already closely aligned such that the local DVC algorithm can effectively resolve displacements at a smaller scale. Without this initial alignment, local DVC may fail to converge or yield unreliable results.

2. **Selection of region of interest:** Not all materials in the sample provided sufficient contrast for correlation. Since the local DVC tracks greyscale patterns in subsets, there must be sufficient variability in greyscale values to make each subset's pattern unique. In both XCT and NCT, the steel exhibited low

spatial contrast in greyscale values, resulting in insufficient information to obtain physically reliable displacement fields. To address this, the steel was masked out from the Region Of Interest (ROI) before performing the local DVC. This was done using a segmentation-based masking, ensuring that only the concrete region was included in the local DVC.

3. **Local DVC:** This step involved computing displacement at a sub-voxel level for subsets within the ROI. The local DVC was an iterative process to determine an appropriate subset size. Larger subsets (i.e. a coarser grid) contain more voxels and thus more distinct greyscale patterns, increasing the likelihood of successful correlation. However, they result in a coarser displacement field due to fewer data points. Conversely, smaller subsets (i.e. a finer grid) provide a higher spatial resolution of the displacement field but are more difficult to correlate because they contain fewer voxels and a greyscale pattern that is less unique. This subset size was therefore selected based on the fraction of converged subsets (the proportion of subsets for which the sum of the squared image residuals satisfied a predefined convergence tolerance) and by validating image residuals. The latter is particularly important, as it provides a qualitative measure of how well the computed displacement field reproduced the deformations in the specimen. This validation was performed by warping the undeformed dataset, using the computed displacement field, and then subtracting the warped dataset from the deformed dataset. The resulting image residual field was analysed to assess how well the displacements had been captured. A successful analysis yields a residual field close to zero, indicating good agreement between the computed and actual displacements. A representative example of the displacement field immediately after local DVC is shown in Fig. 3.4a.

4. **Correction of poorly correlated subsets:** For subsets where correlation failed, the corresponding displacement was interpolated from successfully correlated adjacent subsets using an inverse-distance weighting algorithm [113]. This algorithm assigns weights to the displacement of nearby nodes within a defined radius and computes a weighted average for the displacement of the incorrect subset. Fig. 3.4b shows the displacement field after this correction step.

5. **Filtering of displacement field:** A median filter with a stencil of a defined size was applied to remove large local displacements at individual nodes. This step addressed converged but unreliable displacements in the dataset and was considered as a trade-off due to a somewhat small subset size, which led to higher uncertainties in the computed displacement field. The effect of applying a median filter is illustrated in Fig. 3.4c.

6. **Strain computation:** The strain field was computed from the displacement field obtained through the local DVC (with or without correction of badly correlated subsets and filtering). These displacements were evaluated at the centres of regularly spaced subsets, forming a structured 3D grid. These subset centres, where displacement was defined, were treated as grid nodes for constructing eight-node hexahedral elements used for interpolation. Each element was defined by a $2 \times 2 \times 2$ group of neighbouring subset centres, forming a cube with eight nodes. Within each element, the displacement field was interpolated using trilinear shape functions, and spatial derivatives were computed to obtain the transformation gradient tensor at the element centre [112]. The strain tensor was then derived from this gradient using the infinitesimal strain formulation, yielding a smooth strain field appropriate for the small deformations assumed in this study.

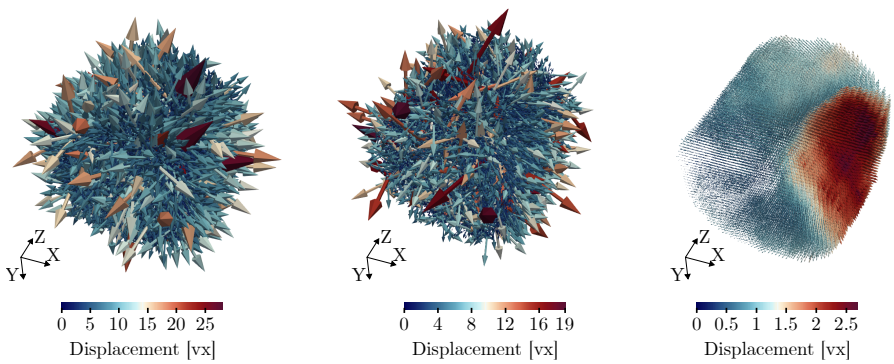

Figure 3.4: Displacement field in the concrete cover resulting from corrosion formation, as obtained through the local DVC analysis. (a) Displacement field directly after local DVC. (b) Displacement field after correction of poorly correlated subsets using inverse-distance weighting. (c) Displacement field after application of median filtering to reduce local noise and smooth isolated outliers. Based on the same datasets and analyses as in [114], figures not previously published.

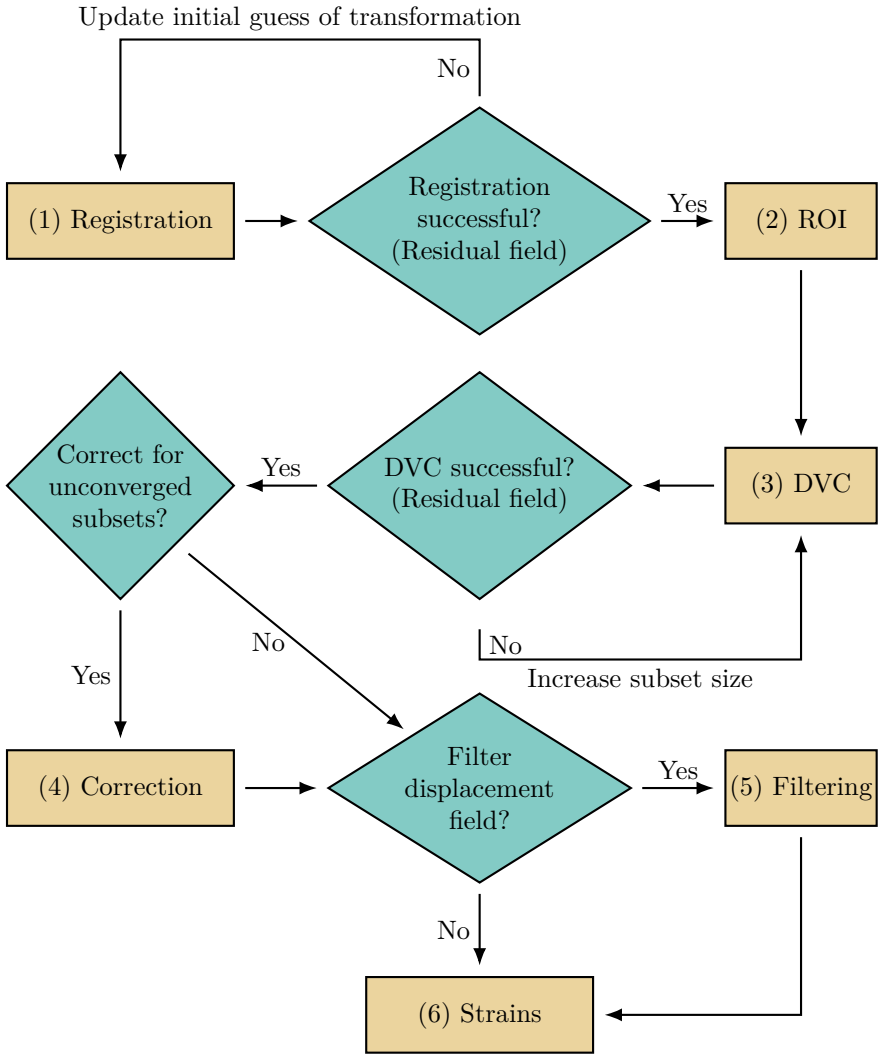

Figure 3.5: Schematic representation of the step-by-step procedure used for DVC analysis.

CHAPTER 4

Summary of research studies

The research studies covered in this thesis can be categorised into two main types: experimental and numerical. One of these studies, fully detailed in **Paper A**, involved the analysis of experimental data from Robuschi et al. [89]. The remaining two experimental studies, presented in **Papers B & C**, were based on dedicated experimental campaigns, each designed, executed and subsequently analysed as part of the research. The final study, presented in **Paper D**, involved Finite Element Analyses (FEA), in which experimental results from **Paper C** were used to inform the model input and boundary conditions. Table 4.1 provides an overview of these studies and their alignment with the research objectives, which are restated below:

- **O1:** To design and execute experimental campaigns for monitoring corrosion and cracking in reinforced concrete at the material scale by integrating tomography and other complementary techniques.
- **O2:** To combine, analyse and interpret data from both experiments and FEA to provide complementary insights into the mechanical effects of steel corrosion in reinforced concrete.
- **O3:** To non-destructively quantify corrosion characteristics and resulting concrete damage.
- **O4:** To investigate the spatial relationship between interfacial voids, corrosion-induced cracks and corrosion morphology.

Table 4.1: Overview of the research studies conducted and how they link to the research objectives.

Appended paper / research study		**A:** Multimodal imaging	**B:** Steel–concrete interface	**C:** Corrosion characteristics	**D:** Mechanics
Technique	XCT	✓	✓	✓	FE modelling
	NCT	✓		✓	
	DOFS		✓		
	ICP-MS			✓	
	Resistance			✓	
Objective	Objective 1		✓	✓	
	Objective 2				✓
	Objective 3	✓	✓	✓	✓
	Objective 4		✓	✓	

Each of the following sections in this chapter presents the research studies conducted. The studies are labelled to correspond with the appended papers. For each study, a brief description of the research, a summary of the key results and reflections are provided.

4.1 Research study A – Multimodal imaging

This study aimed to evaluate the extent to which multimodal X-ray and Neutron Computed Tomography (XCT, NCT) can be used to quantify corrosion characteristics and the associated concrete damage in reinforced concrete. This was achieved by analysing XCT and NCT data acquired at two different time intervals during the corrosion process, which enabled tracking of changes in corrosion and concrete damage between the two stages. This allowed the quantification of kinematics, which would not be possible from a single imaging stage alone. Specifically, this study directly contributed to *Objective 3*, which focused on the quantification of corrosion characteristics and related concrete damage.

Description of experiment

A single reinforced concrete specimen, with geometry illustrated in Fig. 4.1, was subjected to accelerated corrosion through impressed electrical current in two stages, with XCT and NCT scans conducted after each stage. The specimen had a diameter of 31 mm and a length of 130 mm. The Region Of Interest (ROI), which was the volume scanned with XCT and NCT, covered a length of 41.4 mm.

The experimental campaign consisted of two corrosion stages, with XCT and NCT scans conducted after each stage:

- **Stage 1:** Accelerated corrosion was applied at current density of $100\,\mu A\,cm^{-2}$ for 31 d. Following this, imaging data of the specimen were acquired. A corrosion-induced crack was observed at this stage.
- **Stage 2:** The current density was increased to $2985\,\mu A\,cm^{-2}$, which is several orders of magnitude higher than corrosion rates typically measured under natural conditions [10], [115]. To ensure sufficient corrosion development within the limited 24 h beam time, the high current density was applied during part of this period. The specimen was subsequently scanned a second time.

Imaging data of the sample was acquired at the NeXT imaging instrument [100]. The nominal voxel size was 36 µm for the XCT and 26 µm for the NCT. The X-ray source operated with a voltage of 140 kV and a current of 214 µA.

Summary of main results

The study presented a methodology for quantifying kinematics in terms of volumetric strain in the corrosion layer and deformation within the concrete. Since imaging data was acquired at two stages in the corrosion process, changes in material compositions of the different phases present in the sample were linked to the volumetric strain,

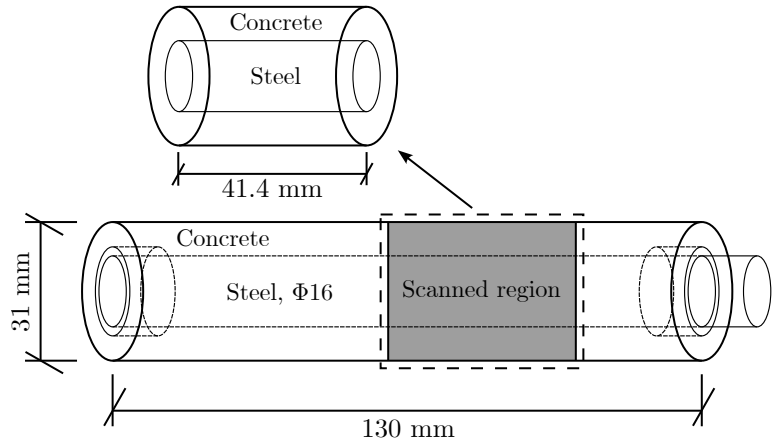

Figure 4.1: Geometry of the specimen investigated in research study A.

and corrosion-induced deformations within the concrete were measured using local Digital Volume Correlation (DVC) [112].

Segmentation of the sample revealed, as expected, an increase in the amount of corrosion products between the first and the second scans. Based on this information, an expression was derived to describe the volumetric strain in the corrosion layer as

$$\varepsilon_v = \frac{V_{cc}}{\eta \Delta V_s - V_{ca}} - 1 \tag{4.1}$$

where V_{cc} is the volume of the compressed corrosion products, η is the free volumetric expansion coefficient of corrosion products, ΔV_s is the loss of steel volume and V_{ca} is the volume of uncompressed corrosion products in the sample.

While the total volume of corrosion products in the sample was quantified from segmentation, the volume of uncompressed corrosion products was estimated by assuming that the reduction in void volume between the first and the second scans corresponded to the accumulation of corrosion products. Consequently, the volume of compressed corrosion products was estimated as the difference between the total and uncompressed volume of corrosion products.

The average volumetric strain in the corrosion layer is plotted as a function of the free volumetric expansion coefficient in Fig. 4.2. As shown, the volumetric strain strongly depends on the expansion coefficient, highlighting the need for accurate quantification of this parameter. For an assumed volumetric expansion of coefficient, $\eta = 3.91$ [89], the average volumetric strain was calculated to $\bar{\varepsilon}_v = -0.72$.

The study also demonstrated that corrosion-induced deformations could be mea-

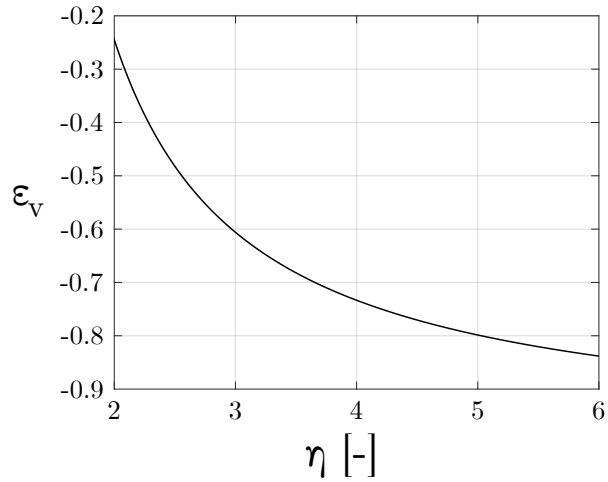

Figure 4.2: Average volumetric strain in the corrosion layer as a function of the free volumetric expansion coefficient of corrosion products. Adapted from **Paper A**.

sured from NCT data. To the best of the author's knowledge, this represents the first instance of such experimental quantification in the 3D space. The ability to non-destructively measure 3D concrete deformations from experimental data represents a novel approach to collecting data that could support, for example, the validation of numerical models simulating corrosion-induced damage in reinforced concrete.

The displacement field is illustrated in Fig. 4.3, where variations in damage within the concrete can be observed. It is important to emphasise that the displacement field measured corresponds to the incremental displacements that occurred due to the second stage of corrosion propagation. This is because the specimen had already undergone some degree of corrosion, albeit to a lesser extent, when the initial XCT and NCT scans were performed.

Fig. 4.4 presents three horizontal sections along the specimen, with a coloured overlay highlighting corrosion products and cracks visible in the NCT data. Below each section, the corresponding distribution of the first principal strain is shown.

Strain localisation was observed in regions of concrete cracking, confirming that the measured concrete deformations were physically relevant. A key finding was that strain localisation was also detected in regions where cracks could not be directly seen in the image data, effectively capturing deformations at a sub-voxel level.

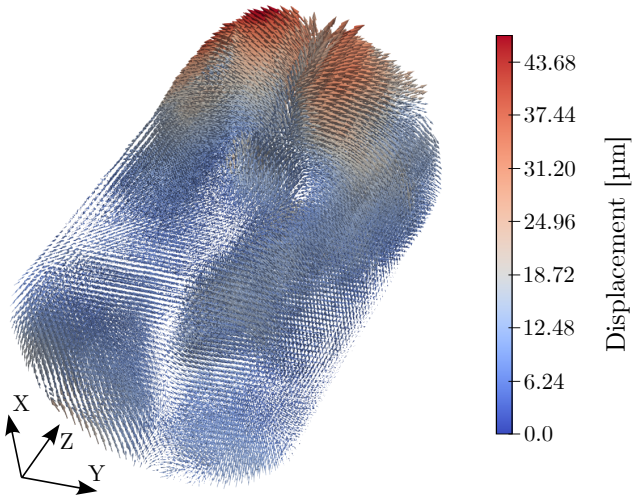

Figure 4.3: Rendering of the displacement field within the concrete cover. Adapted from **Paper A**.

Reflections

Novel outcomes of the present work were the ability to estimate both the volumetric strain in the corrosion layer and to measure corrosion-induced deformations within the mortar using image-based data only. This feasibility study formed the methodological foundation for research study C, described in detail in Section 4.3.

One important reflection is the benefit of acquiring image data at an earlier reference state – ideally prior to the onset of corrosion formation. In the present study, the first scan was conducted after some corrosion had already formed, and splitting cracks had been induced in the concrete cover. As a result, all subsequent measurements had to be interpreted as incremental. This means that absolute quantification of volumetric strain and deformations within the concrete cover, relative to the uncorroded state, was not possible.

Another source of uncertainty concerns the assumption made regarding the transport of corrosion products. The methodology used to estimate the volumetric strain in the corrosion layer relied on quantifying the reduction in interfacial void space between scans, with the assumption that this loss corresponds to the formation of corrosion products. As the imaging only provided data of materials that remain *within* the specimen at the time of scanning, any corrosion products that had been transported away or leached out were not accounted for in the analysis. Improved

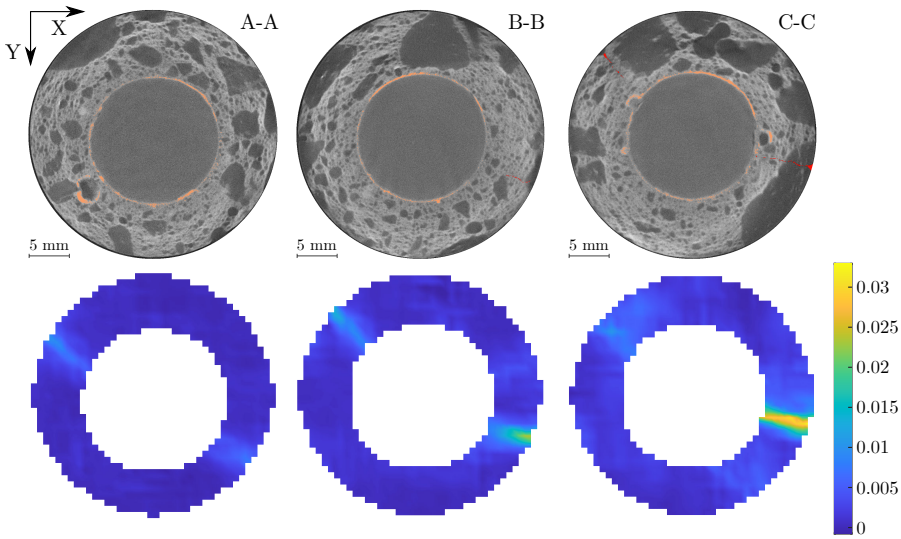

Figure 4.4: Top row: Horizontal NCT slices at three longitudinal positions. Coloured overlay highlight corrosion products (brown) and cracks (red). Bottom row: Corresponding distribution of first principal strain. Reproduced from **Paper A**.

characterisation of this aspect, for example, through chemical analysis of dissolved iron concentrations in the solution in which the specimen is immersed during accelerated corrosion, would further inform the interpretation of volumetric strain values derived from image data.

4.2 Research study B – Steel-concrete interface

As highlighted in research study A, local DVC provided valuable insights into 3D corrosion-induced deformations in concrete. However, it was unable to capture kinematics in the reinforcing steel due to insufficient spatial contrast in the image data. While study A primarily focused on the strain field in the concrete and corrosion layer, research study B explored an alternative approach: directly measuring steel strains during the corrosion process.

To achieve this, Distributed Optical Fibre Sensing (DOFS) was employed to investigate whether monitoring steel strains could offer a new perspective on the Steel-Concrete Interface (SCI) and complement the findings from A. The experimental setup featured cylindrical specimens with embedded hollow steel bars, enabling internal strain monitoring. Optical fibres were mounted on the inner surfaces of the bars, allowing for continuous measurement of steel strains throughout the accelerated corrosion process.

After the corrosion phase, post-mortem XCT was conducted to assess concrete cracking and corrosion morphology. By integrating distributed strain sensing and XCT, this study addressed *Objective 1*, which focused on developing non-destructive experimental campaigns combining multiple techniques at the material scale. In addition, it contributed to *Objective 3* through steel strain measurements, and to *Objective 4* by using XCT to examine the spatial relationships between interfacial voids, corrosion-induced cracks and corrosion morphology. The experimental campaign and its main results are summarised below.

Description of experiment

The experimental campaign included four specimen series, designed to investigate the effects of concrete cover and prior freezing-thawing exposure on the corrosion-induced deformations adjacent to the SCI:

- **C30:** Three specimens (C30a-c) subjected to accelerated corrosion only. Concrete cover: 30 mm.
- **C50:** Three specimens (C50a-c) subjected to accelerated corrosion only. Concrete cover: 50 mm.
- **FC30:** Two specimens (FC30a-b) exposed to freezing and thawing cycles prior to accelerated corrosion. Concrete cover: 30 mm.
- **R30:** Three reference specimens (R30a-c) not exposed to freezing and thawing or accelerated corrosion. Concrete cover: 30 mm.

Each specimen measured 100 mm in length and contained a hollow reinforcement bar of 28 mm outer diameter and 2 mm wall thickness.

The hollow steel bars were fabricated from 32 mm K500C-T reinforcement bars. The ribs were removed by milling, and the hollow section was created using a lathe. The use of hollow steel bars instead of traditional reinforcement served two key purposes:

1. **Enabling internal strain monitoring:** The hollow design made it possible to mount optical fibres on the inner surface, enabling continuous internal strain monitoring throughout the accelerated corrosion process.
2. **Improving XCT image quality:** Reducing the steel volume decreased beam hardening artefacts, thereby improving image quality and easing segmentation.

A continuous strain monitoring was obtained using polyimide-coated optical fibres (sensor diameter: 155 µm) [116]. These fibres were glued in a helical pattern to the inner surface of the hollow bars (Fig. 4.5), ensuring distributed strain measurements along the steel. The fibres were interrogated using an optical distributed sensor interrogator [117] which enabled spatially continuous strain measurements with a resolution of approximately ± 10 microstrain.

The gauge length (i.e., the segment over which strain was averaged) and the measurement rate were initially set to 2.6 mm and 6.25 Hz, respectively. However, these settings were later adjusted to 0.65 mm and 2.08 Hz to improve the quality of the recorded measurements. This adjustment allowed for a higher spatial resolution of the strain data while maintaining a reliable signal. Prior to the corrosion experiment started, a new reference configuration was initialised for each fibre. Hence, all strain measurements presented were relative to the strain at the start of the corrosion phase.

Steel corrosion was induced using an impressed current density of 70 µA cm^{-2} for 41 d. This value was chosen as a compromise between accelerating the corrosion process and maintaining conditions that approximate natural corrosion [10].

Following the corrosion phase, XCT scans were performed to analyse concrete cracking and steel corrosion. The X-ray source operated at 150 kV and 200 mA. The final nominal voxel size was 28.5 µm. Steel corrosion was quantified in terms of the corrosion level, representing the percentage loss in steel cross-sectional area.

Summary of main results

The strain profiles along the optical fibres exhibited fluctuations between extension and contraction throughout the corrosion phase, indicating a non-uniform corrosion morphology, which in turn led to a non-uniform distribution of radial stress at the SCI. Fig. 4.6 presents a typical strain profile for one specimen from each series after one day of accelerated corrosion. The strain variations followed an oscillatory

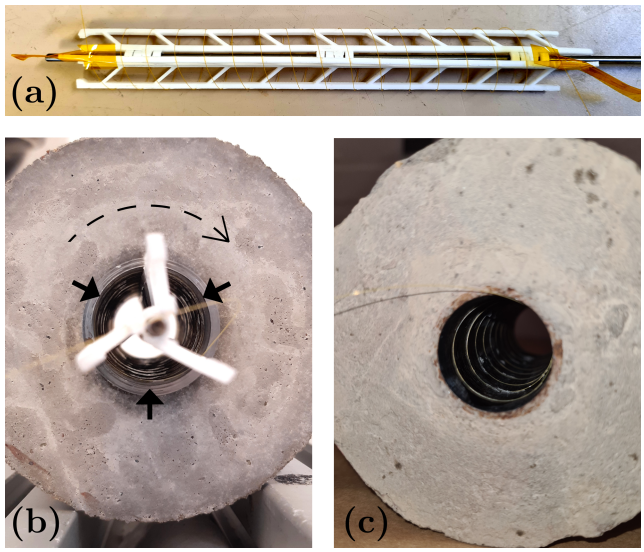

Figure 4.5: Process of gluing the fibre inside the hollow steel bar. (a) Fibre wound around tool arms, restrained with tape. (b) Fibre positioned inside the bar, acquiring a helical shape upon tape removal and tool rotation (dashed arrow). Bonding occurred in gaps between the plastic arms (solid black arrows). (c) Tool removal and additional gluing. Reproduced from **Paper B**.

pattern, alternating between extension and contraction.

Corrosion was most pronounced along distinct bands aligned with dominant cracks in the cover, though some corrosion was also observed across the entire surface of the steel. Additionally, pitting corrosion frequently occurred in regions with interfacial voids. This suggests that both cracking and pre-existing defects at the SCI influence the spatial distribution of corrosion. The cracks likely served as pathways for the ingress of water, oxygen and salts, leading to an increased corrosion activity along these regions. In contrast, interfacial voids may have created localised environments with conditions differing from those in the surrounding cementitious matrix, making regions with interfacial voids more prone to corrosion.

The local strain variations along the optical fibres correlated with the global deformation behaviour, particularly the development of longitudinal cracks and localised corrosion bands, as shown in Fig. 4.7. The hollow steel bars exhibited extension strains in regions corresponding to the dominant crack. This was particularly visible in FC30b (Fig. 4.7f), where strain peaks along the fibre closely followed the

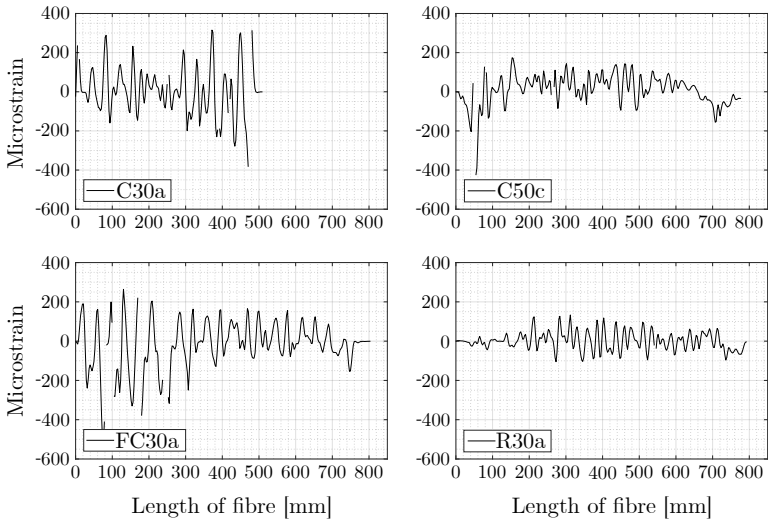

Figure 4.6: Profiles of measured strain for four different specimens after one day of impressed current. Reproduced from **Paper B**.

crack pattern. For C30a (Fig. 4.7e), strain peaks correlated well with cracks for the first three fibre turns but deviated slightly in subsequent turns. This deviation was likely caused by uncertainties in the precise positioning of the fibre, making exact alignment difficult to verify.

Reflections

Despite being subjected to prior freezing and thawing, the FC30 specimens did not exhibit a markedly different corrosion or cracking response compared to the C30 series. This suggests that, under the studied conditions, the impact of freeze–thaw cycling was limited. A likely explanation is that the number of cycles was relatively low, and the specimens may not have reached a critical saturation level required for internal frost damage to develop. Chang et al. [118] highlighted the importance of water boundary conditions in such processes, showing that increased water exposure – particularly full saturation – led to more extensive internal cracking.

For the data presented herein, the extension strains observed at the locations of splitting cracks can be interpreted as a stress relief, since the strain measurements were referenced to the residual stress state prior to corrosion initiation.

Beyond the strain measurements, the novel test setup itself proved to be highly

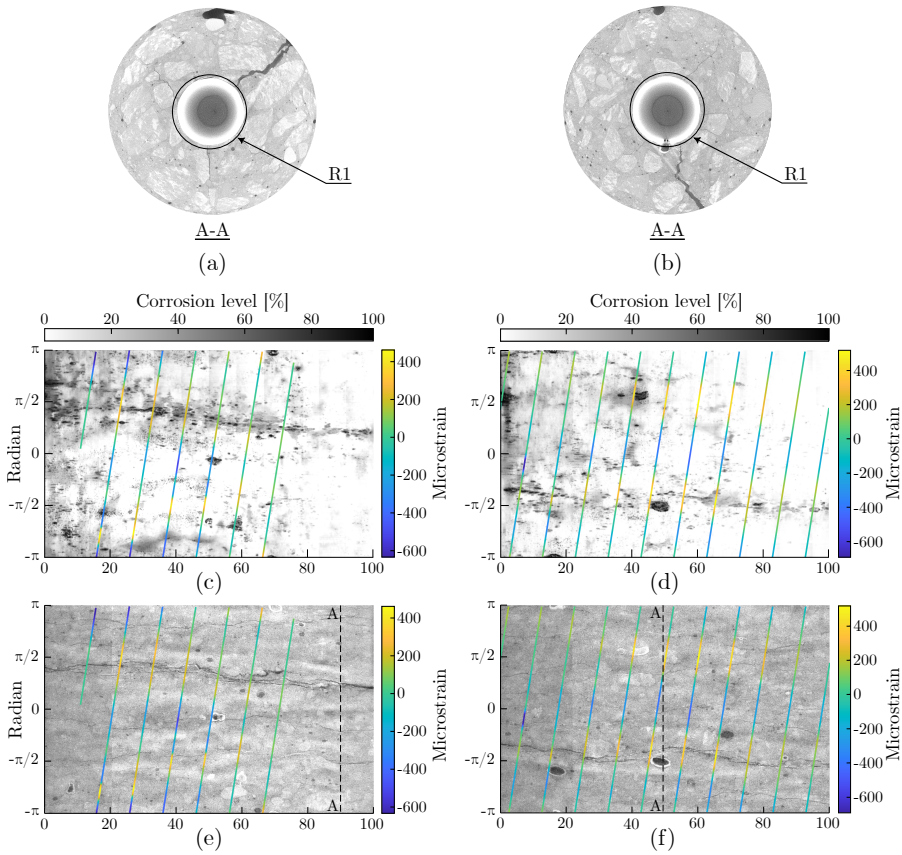

Figure 4.7: Corrosion level and concrete cracking (evaluated from XCT) and strain measurements along the optical fibre shown for C30a (left-hand column) and FC30a (right-hand column). a-b) One horizontal XCT image of each specimen. c-d) Corrosion level and strain measurements at the end of the experiment. e-f) Internal concrete cracking, evaluated at radius R1, and strain measurements. Adapted from **Paper B**.

effective for detailed studies of corrosion and cracking processes in reinforced concrete. By utilising laboratory-made specimens with hollow steel bars at the material scale, the setup enabled non-destructive strain monitoring from within the reinforcement, offering valuable insights into internal deformations during corrosion. These results highlighted the potential of this experimental approach for further studies

on corrosion-induced damage in reinforced concrete. However, further testing using this setup was constrained by practical limitations, including restricted access to the distributed optical fibre sensing equipment, which only supported a limited number of measurement channels (four), and scheduling constraints due to high equipment demand.

An interesting direction that was initially considered involves the potential use of the measured steel strains to estimate the radial stress at the SCI. Given that the strain measurements captured the kinematic response of the steel during corrosion formation, a follow-up inverse analysis or numerical back-calculation could, in principle, be used to estimate the progressive build-up of radial pressure exerted by the expanding corrosion products. However, the feasibility of such an approach would depend on the availability of sufficiently continuous strain data, particularly during the early stages of corrosion, which was partly limited in the present study. To pursue this investigation with greater confidence, a dedicated experimental campaign is advisable, specifically designed for this purpose and focused on ensuring complete data coverage throughout the corrosion process. Nevertheless, the results obtained in this study provide a solid foundation for future developments in this direction.

4.3 Research study C – Corrosion characteristics

This study was designed based on findings and insights from previous research studies, summarised in Sections 4.1 and 4.2, to address knowledge gaps that remained unexamined.

Research study A provided an estimate of the average volumetric strain in the corrosion layer but relied on assumptions about the free volumetric expansion coefficient of corrosion products and the transport of corrosion products through cracks, which were not directly measured. Research study B showed that corrosion localised in regions of cracks and interfacial voids, but the role of void size in pitting corrosion remained unclear. In both studies, tomography data of the initial, uncorroded state of the specimens was not available, requiring assumptions about the reference conditions when interpreting the phase transformations in the specimens.

To address these gaps, research study C aimed to characterise steel corrosion and quantify corrosion-induced damage using a combination of multimodal imaging, analytical techniques and electrical measurements. This research addressed *Objective 1* by combining these techniques, *Objective 3* by quantifying the local free volumetric expansion coefficient of corrosion products, steel loss, corrosion morphology and volumetric strain in the corrosion layer, and *Objective 4* by analysing the risk of corrosion in interfacial voids and the influence of their size.

Description of experiment

The experiment consisted of two series, each designed to address different research questions. The first series included two reinforced mortar specimens (NX10B and NX10C), which were scanned with XCT and NCT. The second series comprised six specimens (TC10B1-3 and TC10C1-3) and the experiment was designed to investigate the transport of corrosion products in relation to mortar cracking.

A combination of complementary techniques was employed to quantify corrosion and its related matrix damage:

- **Multimodal XCT and NCT:** Tomography data were acquired for specimens NX10B and NX10C both before and after accelerated corrosion.
- **Electrical resistance monitoring:** The electrical resistance of the specimens was continuously recorded throughout the corrosion process by measuring of the potential difference.
- **ICP-MS:** Inductively Coupled Plasma Mass Spectrometry (ICP-MS) was used to measure the concentration of iron isotopes in the surrounding water during the corrosion process for specimens TC10B1-3 and TC10C1-3.

The specimen geometry was designed to achieve a balance between sufficient image resolution and structural representativeness. Each specimen was cylindrical, with a

diameter of 26 mm and a length of 30 mm, embedding a centrally placed plain steel bar (6 mm in diameter). The steel bar protruded 10 mm from one end to facilitate electrical connection during the corrosion process, while the opposite side was fully embedded, providing a 5 mm mortar cover.

Two mortar mixes (mortar B and mortar C) were used. The mix compositions were prepared with salts to prevent the formation of a passive layer around the steel bars. Mortar B, used for specimens NX10B and TC10B1-3, contained 3 % sodium bromide (by mass of cement) while mortar C, used for specimens NX10C and TC10C1-3 contained 3 % of sodium chloride (by mass of cement). The selection of different salts was based on their different neutron attenuation properties. Sodium bromide attenuates neutrons less than sodium chloride [91], thereby reducing image noise in the NCT.

The corrosion rate was controlled by applying a constant current density of 50 µA cm^{-2}. A separate galvanic cell was established for each specimen, for which the electrical potential was monitored by continuous readings. For NX10B and NX10C, electrical current was applied for slightly less than 100 h, as a decrease in electrical resistance indicated cracking of the mortars. For TC10B1-3 and TC10C1-3, corrosion was applied for a longer period, as the aim was to investigate transport of corrosion products in relation to the time to cracking.

XCT and NCT of specimens NX10B and NX10C were conducted at the NeXT imaging instrument [100], both before and after the corrosion process, at 77 d and 245 d after casting, respectively. To prevent drying shrinkage during this period, the specimens were kept immersed in water. The nominal voxel size was 16.8 µm for NCT and 18.7 µm for XCT. The X-ray source was configured with a voltage of 140 kV and a current of 130 µA.

ICP-MS was used to quantify the concentration of Iron-57 in the surrounding water during the corrosion process, thus providing insights into the transport of corrosion products in relation to cracking of the mortars.

For NX10B and NX10C, a single water sample was collected at the end of the corrosion process. In contrast, for TC10B1-3 and TC10C1-3, water samples were collected at regular intervals throughout the process. Prior to the corrosion process started, an initial water sample was taken from each specimen to measure the initial concentration of Iron-57 in the water, followed by periodic sampling during the corrosion process.

To ensure a representative measurement, the water surrounding each specimen was carefully mixed before sampling. The collected samples were diluted (1:25) with deionised water, and nitric acid was added to fully dissolve any corrosion products. Samples were then sealed and stored at 8 °C until the ICP-MS analysis was carried out.

Summary of main results

The corrosion morphology observed in specimens NX10B and NX10C were found to be non-uniform, as illustrated in Fig. 4.8. Corrosion was more pronounced in regions adjacent to cracks and where interfacial voids were present, corroborating the findings from research study B. For NX10C, corrosion was localised between two cracks rather than directly at the crack positions.

The influence of interfacial voids on localised corrosion was further examined with respect to the volume of the interfacial voids. These voids were segmented, labelled and ranked by size. Although not every void contained corrosion, corrosion was present in almost all regions containing voids larger than 0.2 mm^3.

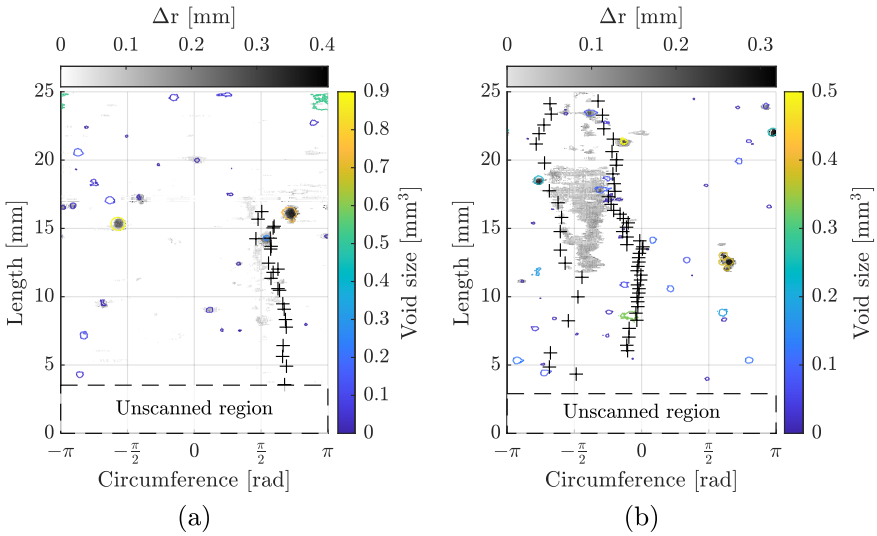

Figure 4.8: Loss in steel radius (greyscale), interfacial voids (coloured) and mortar cracking at the steel-mortar interface (plus signs) for (a) NX10B and (b) NX10C. Plotted size of the voids corresponds to the contact area with the steel while the colour represents their total volume. Adapted from **Paper C**.

The free volumetric expansion coefficient of corrosion products was estimated by analysing the bulk volume of corrosion products within interfacial voids and the corresponding volume loss of the adjacent steel. A similar trend was observed in both specimens, with only a slight variation between them. The estimated coefficients were 3.90 for NX10B and 3.84 for NX10C.

The transport of corrosion products was observed to be delayed relative to mortar cracking, as shown in Fig. 4.9 for TC10C1-3. A delay was observed for all specimens between crack initiation and the first measurable increase in Iron-57 concentration in the surrounding water, which occurred a few days after cracking. The concentration of Iron-57 in the surrounding water generally began to increase when corrosion products became visible to the naked eye. At the time of the second tomography scan, the concentration of Iron-57 in the water remained low for both of the scanned specimens, confirming that corrosion products remained in the sample.

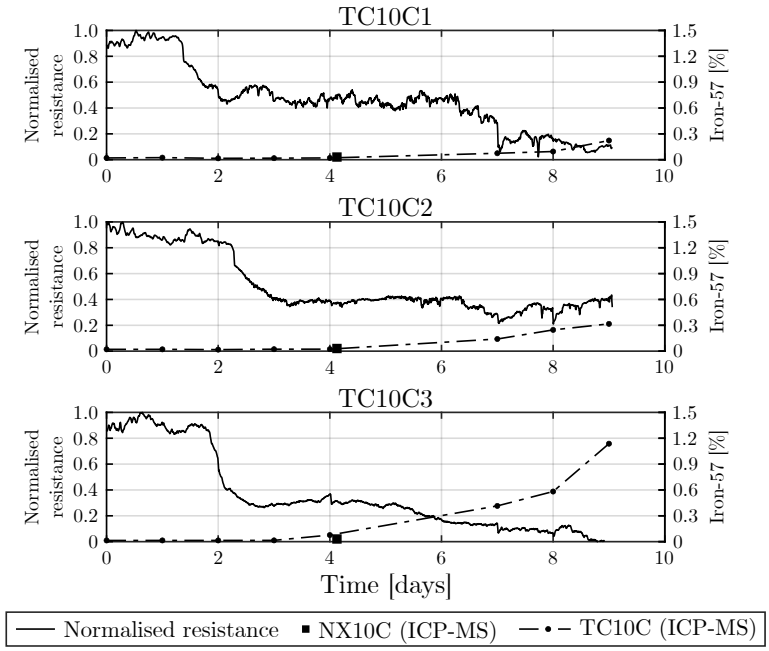

Figure 4.9: Normalised electrical resistance and Iron-57 concentration in the water surrounding specimens TC10C1-3 as a function of time. Adapted from **Paper C**.

Reflections

The volumetric expansion coefficient of corrosion products is a key parameter for modelling corrosion-induced cracking in reinforced concrete, as it governs the internal pressure build-up at the Steel-Mortar Interface (SMI). In this thesis, image-based

measurements yielded coefficients of 3.84 and 3.90, which compare well with previous studies of accelerated corrosion. Robuschi et al. [89] reported a value of 3.91, while Sun et al. [119] found 3.90. Slightly higher values have been observed for natural corrosion (e.g., 4.13–4.24 [89]). These values imply the presence of corrosion phases such as $Fe(OH)_2$ or $Fe(OH)_3$ ($\eta \approx 3.75 - 4.1$) [26].

In contrast, X-ray diffraction studies, which identify mineral phases post-extraction, tend to report lower expansion coefficients in the range of 2.6–3.2 [17], [120]. This highlights differences in methodology: while image-based techniques, on the one hand, capture in-situ volumetric changes, including corrosion expansion into interfacial voids, they provide no information on mineralogy. Diffraction methods, on the other hand, offer chemical identification but may alter the corrosion products during drying and exposure to oxygen [71], [121], and subsequently the volumetric expansion coefficient.

In addition to methodological differences, the local environmental conditions during corrosion formation may also contribute to the observed variation. Since the volumetric expansion coefficients in this study were derived from corrosion products accumulated in interfacial voids, where the oxygen availability is likely higher than in more confined regions along the interface, the formation of more porous and expansive phases may have been favoured [71]. This may partly explain the relatively high expansion coefficients observed in this study.

Another key observation across the experimental studies was the non-uniformity of corrosion morphology. Localised (pitting) corrosion was observed where interfacial voids were present, with nearly all voids larger than $0.2\,mm^3$ containing pitting corrosion. These findings align with earlier work identifying interfacial voids as preferential sites for corrosion initiation [122], [123].

While a spatial investigation between corrosion and voids was performed, the governing electrochemical conditions, such as local oxygen level, moisture content [124] and chloride concentration [123], were not measurable from the image data. However, neutron imaging has shown potential for detecting water distribution in cementitious matrix [125], [126], but the image noise in the present neutron data, largely due to specimen saturation, limited further interpretation in this regard.

Moreover, characterisation of the Corrosion Accommodating Region (CAR) was not possible. The resolution of the imaging data, combined with residual beam hardening artefacts near the SMI, limited the ability to detect small-scale porosity variations that could indicate the presence of such a region. Additionally, since image data were acquired only at two discrete time points (before and after the onset of corrosion-induced cracking), it was not possible to analyse the progressive accumulation of corrosion products at the SMI in relation to the development of deformations in the surrounding mortar.

4.4 Research study D – Mechanics

While the imaging approach adopted in research study C provided detailed insights into corrosion characteristics and mortar damage, it could not directly reveal the internal stress state responsible for crack initiation and propagation. To brigde this gap, research study D employed non-linear FEA to investigate the mechanics of corrosion-induced cracking in reinforced mortar.

The aim was to evaluate the internal mechanical response; specifically, the radial stress at the SMI resulting from the formation of steel corrosion. To this end, the finite element model was informed by detailed experimental data from study C, including spatially varying corrosion characteristics such as corrosion penetration depth, corrosion morphology, volumetric expansion coefficient of corrosion products, volumetric strain in the corrosion layer as well as detailed information about crack pattern and interfacial voids. The volumetric expansion coefficient of corrosion products was assumed to be constant along the interface. These data enabled the finite element model to closely replicate the conditions of the experimentally tested NX10C specimen.

By integrating these experimentally derived inputs, the study extended the findings of research study C by providing an estimate of the radial stress exerted at the SMI due to steel corrosion. This work contributed to *Objective 2*, by combining experimental and numerical data to assess the mechanical effects of steel corrosion, and to *Objective 3*, by providing a quantitative estimate of the stresses driving corrosion-induced cracking.

Description of the finite element model

The FEA was conducted in DIANA FEA 10.9 [127]. The geometry of the model corresponded to the reinforced mortar specimen NX10C from research study C. While the experimental specimen consisted of a centrally embedded plain steel bar (6 mm in diameter) within a cylindrical mortar specimen (26 mm in diameter and 30 mm in length), only the mortar was explicitly modelled. Experimental image data of the corrosion characteristics were used to back-calculate the normal displacement field at the SMI, which was then applied as prescribed nodal boundary conditions in the analyses. An overview of the model is shown in Fig. 4.10a.

Mortar

The mortar domain was discretised using 3D structural solid elements. The element types primarily consisted of 8-noded isoparametric hexahedral elements, although additional element types were included to accommodate the circular geometry: 5-node pyramids, 6-node prisms and 4-node tetrahedra.

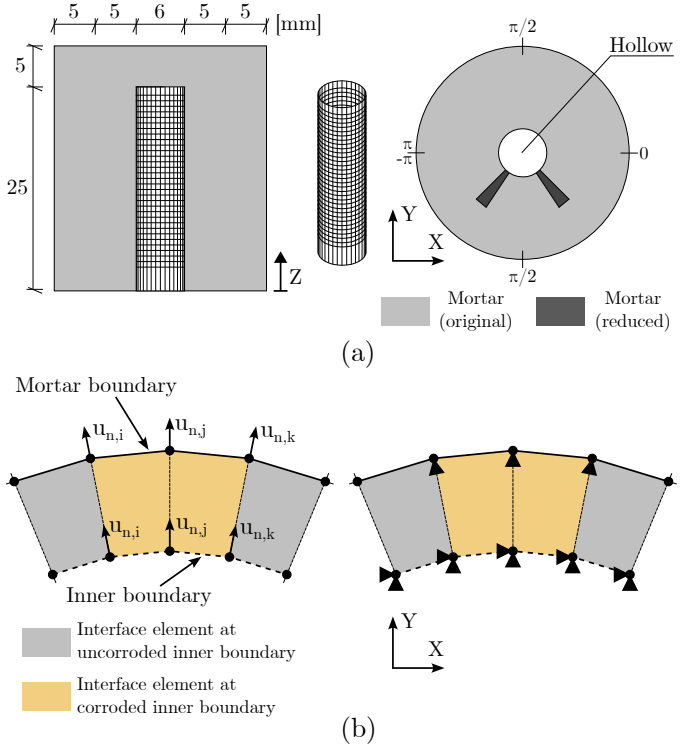

Figure 4.10: Geometry and boundary conditions of the finite element model. (a) Geometry of the reinforced mortar specimen, including the discretisation of the boundary surface, and (b) overview of prescribed nodal displacements and boundary conditions. Adapted from **Paper D**.

To provoke localised cracking, reduced material properties were assigned to elements adjacent to the SMI, based on the experimentally observed positions of cracks at the SMI. These material properties were assumed to be 40 % of the original mortar.

The mortar was modelled using non-linear fracture mechanics. A smeared crack approach was used to represent tensile cracking [128], [129], while the compressive behaviour was assumed to be linear elastic, perfectly plastic to avoid mesh-sensitive crushing [130].

Steel-mortar interface

A boundary surface, representing the steel surface area, was modelled using 2D elements. The surface was discretised with a polygonal mesh consisting of 32 divisions along the circumference and 33 along the longitudinal axis, and was treated as a boundary surface in the analysis. This modelling choice was based on the assumption that the steel, due to its much higher stiffness, undergoes negligible deformation compared to the surrounding mortar. As a result, the internal deformations of the steel were assumed to be negligible.

To model the mechanical interaction between steel and mortar, structural plane interface elements were assigned at the SMI. For the normal stiffness, a bilinear relationship between the normal stiffness and relative displacement was assumed: a higher stiffness was applied in compression and a lower in tension. This bilinear formulation was introduced to ensure effective transmission of compressive stresses across the interface, while simultaneously limiting the interface's ability to carry tensile stresses.

All stiffness parameters were selected based on the results of a Full Factorial Design (FFD), in which the influence of normal and shear stiffnesses (longitudinal and tangential to the boundary surface) on mortar cracking and the radial stress at the SMI was investigated. The results from this analysis showed that the interface stiffness parameters had a negligible influence on the radial stress, whereas the normal stiffness in compression had a significant impact on the scaling factor of the applied load at which surface cracking occurred. The selected values for the normal stiffness in tension and compression were $D_{n,t} = 3 \times 10^{10}\,\mathrm{N\,m^{-3}}$ and $D_{n,c} = 3 \times 10^{12}\,\mathrm{N\,m^{-3}}$, respectively. The shear stiffness along and around the boundary surface was set to $D_l = D_t = 1 \times 10^{11}\,\mathrm{N\,m^{-3}}$.

Loads and analysis details

The expansive effect of steel corrosion was represented in the model by applying prescribed radial displacements to nodes located at the SMI, corresponding to the corroded regions. These displacements were estimated from spatially resolved measurements of the volumetric strain in the corrosion layer and corrosion penetration, as obtained in research study C.

To convert the volumetric strain into nodal displacements, an analytical expression originally formulated by Lundgren [68] was used. The expression relates the strain in the corrosion layer as the ratio between its actual radial expansion and the thickness of the corrosion layer under free expansion.

In this study, it was assumed that the strain in the corrosion layer at each location, $\varepsilon_{cor,i}$, was equal to the experimentally measured volumetric strain at each location, $\varepsilon_{v,i}$. This simplification implies that the corrosion products expand pre-

dominantly in the direction normal to the steel surface, with minimal expansion along the circumference and longitudinal directions. While this assumption is considered reasonable for relatively uniform corrosion morphologies, it may be less valid in cases of highly localised attacks, where the expansion may be more uneven and not confined to the radial direction.

Based on this assumption, the original formulation was rearranged to solve for the radial displacement at each node i along the SMI:

$$u_{n,i} = \varepsilon_{v,i}(x_i + a_i) + a_i - f_i \tag{4.2}$$

Here, x_i is the local corrosion penetration depth, f_i is the thickness of an interfacial void at node i and a_i is the free radial expansion under zero stress. The value of a_i was computed based on the free volumetric expansion coefficient $\eta = 3.84$ (assumed constant) and x_i, using an expression from Lundgren [68]:

$$a_i = -r + \sqrt{r^2 + (\eta - 1) \times (2rx_i - x_i^2)} \tag{4.3}$$

where r is the initial radius of the steel.

In regions where a void was present ($f_i > 0$), the prescribed displacement was thus reduced accordingly, reflecting the assumption that corrosion products in these regions could expand into the void space before generating pressure on the surrounding mortar. In cases where f_i was sufficiently large to result in a negative value of $u_{n,i}$, the displacement was set to zero, corresponding to the assumption that corrosion products could expand entirely within the void space without inducing stress on the mortar.

Two cases were investigated, differing in whether the effect of interfacial voids was included in the analysis:

- **Case 1:** Prescribed nodal displacements according to Fig. 4.11a and $f = 0$.
- **Case 2:** Prescribed nodal displacements with $f > 0$ (Fig. 4.11b-c).

Because interface elements were used to model the interaction between the mortar and the boundary surface, each location along the interface consisted of two coincident nodes: one belonging to the mortar domain and the other with the boundary surface. The prescribed radial displacement in corroded regions was applied equally to both nodes, as illustrated in Fig. 4.10b.

In both modelling cases, the nodes on the boundary surface were fully constrained in all spatial directions. In contrast, mortar nodes in corroded regions were restrained only in the radial direction, allowing them to move freely along the longitudinal and transverse directions. In uncorroded regions, no constraints were applied to the mortar nodes, enabling these nodes to deform freely in response to the overall structural response. The prescribed nodal placements were applied in

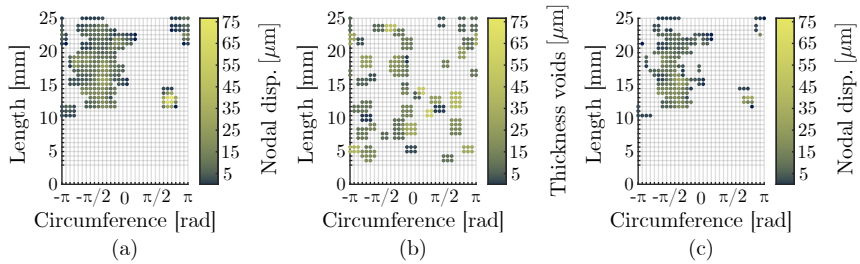

Figure 4.11: Nodal representation of normal displacement and interfacial voids. (a) the normal displacement of the interface without accounting or interfacial voids (Case 1) (b) thickness of interfacial voids at each node (c) normal displacement of the interface, accounting for the presence of interfacial voids (Case 2). Adapted from **Paper D**.

a displacement-driven analysis, using a linear ramp over 50 incremental steps. At each step, global equilibrium was established through a Newton-Raphson iterative solution scheme.

In addition to corrosion-induced displacements, autogenous shrinkage of the mortar was incorporated in the model. It was assumed that the primary effect of autogenous shrinkage occurred before the onset of corrosion. The autogenous shrinkage strain was set to $\varepsilon_{ca} = 0.056$ ‰, based on an empirical expression provided in [53], which relates autogenous shrinkage to the strength class of the mortar.

Summary of main results

The distribution of radial stress at the SMI for both load cases is shown in Fig. 4.12. In both scenarios, higher compressive radial stresses developed predominantly in regions affected by significant corrosion.

When interfacial voids were not considered (Fig. 4.12a), the maximum compressive stress exceeded 12 MPa. In contrast, when the influence of interfacial voids on the prescribed nodal displacement was included (Fig. 4.12b), fewer nodes were actively constrained, and the imposed displacements became more spatially heterogenous. This led to local stress concentrations in the remaining regions were displacement was still prescribed, with compressive stresses reaching approximately 15 MPa. These results demonstrate that the local stress at the SMI is not solely governed by the magnitude of the expansion, but is strongly influenced by the corrosion morphology and the presence of interfacial voids.

In both cases, smaller tensile radial stresses were observed adjacent to and within corroded regions. These arose from local deformation compatibility; when neigh-

bouring nodes are subjected to different prescribed displacements, the mortar deforms continuously, causing regions with less corrosion to experience addition deformation and consequently tensile stresses. This effect was more pronounced when the thickness of interfacial voids was accounted for, as the reduction in prescribed displacements increased the displacement gradients across the interface. As a result, tensile stresses reached up to 3.7 MPa in the case with voids considered (Fig. 4.12b), compared to a maximum of 1.7 MPa in the case without this consideration (Fig. 4.12a).

Moreover, since corrosion was predominantly concentrated on one side of the bar, the imposed expansion was asymmetric. Due to equilibrium, smaller compressive stresses on the opposite side of the bar developed, despite the absence of any imposed displacements in those regions.

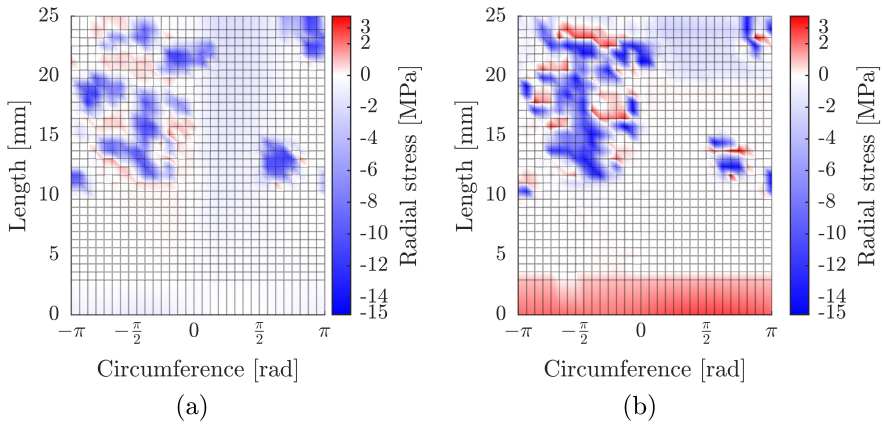

Figure 4.12: Distribution of radial stress at the SMI, shown as a function of the circumference and longitudinal positions along the steel. (a) Without accounting for the effect of interfacial voids on the prescribed normal displacement. (b) With the correction for interfacial voids included. Reproduced from **Paper D**.

To explore the mechanical behaviour of the corrosion layer, the computed radial stress values were compared against the image-based experimentally determined volumetric strains. The results for both loading cases are presented in Fig. 4.13.

Most of the data points corresponds to volumetric strains typically ranging between –0.5 to –0.7 and associated with radial stresses spanning from approximately +1.5 MPa in tension to –5 MPa in compression. A limited number of points exhib-

ited substantially higher compressive stresses, with peak values reaching –12.2 MPa and –14.7 MPa in the respective analyses. These local peaks in compressive stress occurred primarily in regions of localised corrosion or near the boundaries of corroded regions, as can be seen in Fig. 4.12.

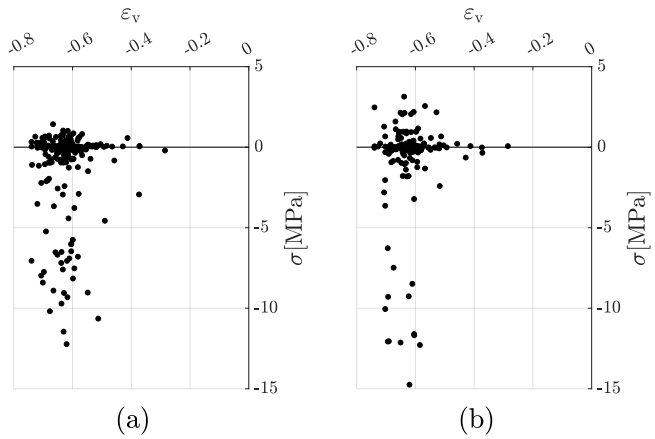

Figure 4.13: Scatter plots illustrating the relationship between radial stress and volumetric strain in the corrosion layer. (a) Without consideration of interfacial voids in the nodal displacement. (b) With consideration of interfacial voids. Reproduced from **Paper D**.

Reflections

The results shown in Fig. 4.13 suggest that the corrosion products do not behave in a linearly elastic manner. Instead, the relationship between volumetric strain and radial stress was qualitatively similar to trends seen in granular materials under confined conditions, where stiffness increases with compaction. This behaviour is consistent with experimental observations of the mechanical behaviour of corrosion products under compression, as compiled in Fig. 2.2 from the works of Ouglova et al. [76], Zhao et al. [73], Xu et al. [77] and the early estimation by Lundgren [68].

Some variability was observed in the stress-strain results, including instances where compressive volumetric strains were associated with tensile radial stresses. This outcome is linked to the modelling approach: while the interface was not completely incapable of carrying tensile stresses, its tensile stiffness was set to lower than in compression to reflect the weaker bond in tension. Despite this, the tensile radial stresses were relatively high in the corrosion layer. In future work, it may

be relevant to assign different values of the normal stiffness in tension for corroded and uncorroded regions at the SMI, in order to better reflect the assumption that corrosion products do not carry tensile stresses.

It is also relevant to reflect on the relatively large volumetric strain obtained from the experimental characterisation. As shown earlier in Fig. 4.2, the volumetric strain increases non-linearly with the volumetric expansion coefficient, leading to large strain magnitudes for higher coefficients. Given the large expansion coefficient for the corrosion products in the studied specimen (3.84), the volumetric strain would theoretically approach $\varepsilon_v \approx -0.74$ in an idealised case where no deformation occurs at the SMI.

Moreover, the volumetric strain in the corrosion layer may also be influenced by expansion in directions along and transverse the bar. This is particularly likely near the edges of corroded regions, where the corrosion products could expand not only radially but also longitudinally and tangentially. Incorporating these directional effects in future modelling efforts may reduce the number of data points showing tensile stresses under compressive strain and may also help to reduce the observed scatter.

CHAPTER 5

Conclusions and future work

The overarching aim of this thesis was to characterise steel corrosion and the resulting damage in reinforced concrete at the material scale using tomographic techniques. The material scale referred to specimens with diameters ranging from 26 mm to 88 mm, designed to achieve image data at micro-scale. This chapter begins with a graphical summary of the research, followed by conclusions structured according to the research objectives. Finally, suggestions for future work are presented.

5.1 Graphical summary of the research approach and outcomes

Fig. 5.1 provides an overview of the research structure, highlighting how the individual studies contribute to the overall research objectives. Each research paper addressed one or more of the defined objectives, as indicated in the figure.

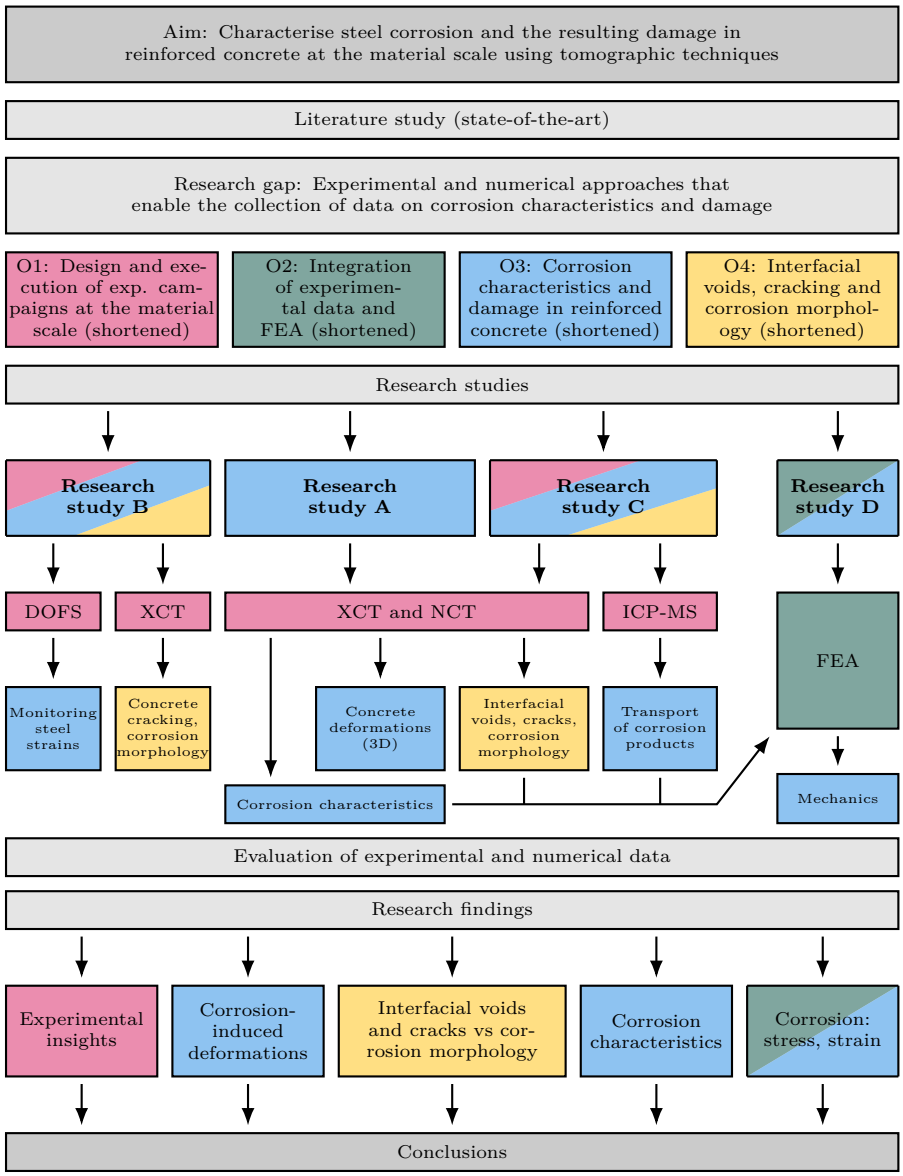

Figure 5.1: Overview of the research structure, illustrating the alignment between research objectives, methodologies and main outcomes.

5.2 Conclusions

This section presents the main conclusions of the research, structured according to the four objectives defined in Section 1.2.

O1: Design and execution of experimental campaigns

Two independent experimental campaigns were designed and executed to investigate steel corrosion and cracking in reinforced concrete at the material scale. These campaigns combined non-destructive and non-invasive X-ray Computed Tomography (XCT), alone or in a multimodal approach with Neutron Computed Tomography (NCT), with complementary techniques to complete dataset. These complementary techniques included electrical resistance measurements, Inductively Coupled Plasma Mass Spectrometry (ICP-MS) and Distributed Optical Strain Sensing (DOFS).

- Tomographic imaging enabled detailed characterisation of corrosion penetration depth, morphology and associated crack patterns from single scans. Through repeated scanning of the same specimen, the method also enabled quantification of the volumetric expansion coefficient and the volumetric strain in the corrosion layer – establishing a novel, non-destructive approach to quantify key parameters relevant for modelling corrosion-induced cracking in concrete.
- Local Digital Volume Correlation (DVC) was demonstrated on NCT data to enable the measurements of 3D corrosion-induced deformations within the cementitious matrix.
- Monitoring of the iron isotope concentrations in the surrounding water using ICP-MS during the accelerated corrosion process, in combination with electrical resistance measurements, highlighted the relationship between the outward transport of corrosion products and mortar cracking.
- DOFS enabled direct measurements of corrosion-induced steel strains. Integrated with XCT, it revealed the spatial relationship between steel deformations, concrete cracking and corrosion morphology.

O2: Integrating experiments and FEA

Image-based data were combined with finite element modelling to estimate internal mechanical quantities not accessible through imaging alone, such as radial stress at the steel–mortar interface.

- The integration of experimental and numerical research was critical for advancing the understanding of the mechanics associated with steel corrosion

in reinforced concrete. Neither imaging nor numerical modelling alone could provide a complete understanding; rather, their integration enabled complementary insights into the processes and mechanisms involved in steel corrosion in reinforced concrete.

- A central contribution was the direct integration of image-based experimental data – including corrosion morphology, penetration depth, volumetric strain in the corrosion layer and crack patterns – into the finite element model. This enabled evaluation of internal mechanical quantities, such as radial stress at the steel-mortar interface, which cannot be obtained through image processing alone.
- The analysis indicated a non-linear mechanical response of the corrosion layer, consistent with trends reported in the literature.

O3: Corrosion characteristics and damage

Quantitative image analyses were performed on corroded specimens to characterise corrosion and the resulting damage in the surrounding concrete.

- The free volumetric expansion coefficient of corrosion products was quantified in two specimens, yielding consistent values of 3.90 and 3.84, respectively. These values are in close agreement with those reported in previous image-based studies, although somewhat higher than values obtained using alternative experimental methods.
- The volumetric strain in the corrosion layer was estimated in two independent studies. In one, the average strain across the entire sample was $\bar{\varepsilon}_v = -0.72$. In the other, the volumetric strain was spatially resolved along the circumference and length of the steel, with values ranging from approximately -0.5 to -0.7. Together, these results indicate a substantial volumetric compaction of the corrosion products due to confinement at the interface.
- Corrosion-induced longitudinal cracks in the concrete cover were observed in all specimens. These cracks were further analysed using a local DVC, which revealed strain localisation in regions where no cracks were yet visible in the image data. This demonstrates that advanced image-based analysis can measure early-stage damage at the sub-voxel level – capturing mechanical deterioration before cracks become visually distinguishable in the image data.
- Circumferential steel strains caused by the formation of corrosion products were found to be highly non-uniform, with extension strains concentrated near and across concrete cracks and contraction strains in between.

O4: Spatial relationship between corrosion morphology, interfacial voids and cracks

Spatial correlation analyses were performed between image data of corrosion penetration, morphology, interfacial voids and cracks, to investigate where corrosion is likely to initiate.

- Corrosion penetration was generally larger in regions located near concrete cracks, indicating a spatial correlation between cracking and corrosion morphology. This pattern likely results from increased access to oxygen, water and chlorides through the cracks, which are necessary for corrosion to develop.
- Pitting corrosion was most frequently observed in regions containing interfacial voids. In these regions, the steel corrosion penetration was typically greater inside the void and lower or along its edge or in adjacent areas.
- Larger interfacial voids were strongly associated with pitting corrosion, indicating that void size is a critical parameter influencing the risk of localised corrosion.

5.3 Suggestions for future research

This thesis focused on characterising steel corrosion and the resulting concrete damage using imaging data acquired at distinct points in time. While effective for quantifying corrosion characteristics and associated damage, this approach was limited by the temporal resolution of the image data. As a result, the detailed *evolution* of corrosion and cracking remains largely unexplored. Certain assumptions were therefore necessary to interpret how these processes progressed between scans.

One particularly interesting observation relates to the spatial relationship between corrosion morphology, interfacial voids and cracks. The results presented in this thesis showed that pitting corrosion occurred frequently in interfacial voids, and that the likelihood of corrosion appeared to increase with the void size. While these findings suggest a strong geometric influence, more frequent imaging during the corrosion process could help clarify how corrosion localises and evolves within and around interfacial voids over time.

Another promising direction concerns the integration of experimental data into finite element modelling. In this thesis, experimentally derived inputs including corrosion morphology and penetration depth, volumetric strain in the corrosion layer and concrete cracking were used to inform a finite element model aimed at estimating the mechanical response associated with steel corrosion. Future work could build on this framework by incorporating the time-dependent progression of steel corrosion into the model. To support this, a logical next step would be to conduct experiments

that capture how steel corrosion and related damage develop in real time through *in-situ* (operando) imaging.

In-situ experiments would enable full-field 4D characterisation (three spatial dimensions plus time). Beyond providing insights into the evolution of steel corrosion and concrete cracking, such experiments would support the development of more physically realistic numerical models. By capturing how corrosion morphology and penetration depth develop over time, the resulting image data could serve as both independent dataset for model validation and as a basis for inverse modelling strategies. Such image-based modelling approaches would help constrain model parameters and ensure consistency with experimentally observed behaviour. This would not only reduce uncertainty in the mechanical response, but could also support the future development of performance indicators that reflect internal corrosion damage and are suitable for on-site assessment of reinforced concrete structures.

Finally, imaging in this thesis was conducted using laboratory-based XCT systems and neutron imaging at large-scale facility, with spatial resolutions on the order of tens of microns. Future studies could benefit from imaging approaches that offer both higher spatial resolution and scan times. In particular, the capabilities of imaging instruments at 4^{th} generation synchrotron sources should be more carefully exploited. The combination of sub-micron spatial resolution, fast scan times and propagation-based phase contrast allows for truly high-resolution imaging of small-scale (centimetre) samples by employing hierarchical tomography techniques [131].

References

[1] J. Wight, *Reinforced concrete Mechanics and Design*. Pearson Eductional Limited, Edinburgh Gate, England, 2016.

[2] A. Poursaee and C. Hansson, "Potential pitfalls in assessing chloride-induced corrosion of steel in concrete," *Cement and Concrete Research*, vol. 39, pp. 391–400, 2009. DOI: 10.1016/j.cemconres.2009.01.015.

[3] L. Bertolini, B. Elsener, P. Pedeferri, and R. Polder, *Corrosion of Steel in Concrete: Prevention, Diagnosis, Repair*. Wiley-VCH verlag GmbH & Co. KGaA, Weinheim, Germany., 2004. DOI: 10.1002/3527603379.

[4] M. Stewart and A. Al-Harthy, "Pitting corrosion and structural reliability of corroding RC structures: Experimental data and probabilistic analysis," *Reliability Engineering & System Safety*, vol. 93, pp. 373–382, 2008. DOI: 10.1016/j.ress.2006.12.013.

[5] E. McCafferty, *Introduction to Corrosion Science*. Springer New York Dordrecht Heidelberg, London, United Kingdom, 2010. DOI: 10.1007/978-1-4419-0455-3.

[6] C. Hansson, "The Impact of Corrosion on Society," *Metallurgical and Materials Transactions A*, vol. 42, pp. 2952–2962, 2011. DOI: 10.1007/s11661-011-0703-2.

[7] R. Polder, G. Leegwater, D. Worm, and W. Courage, "Service life and life cycle cost modelling of cathodic protection systems for concrete structures," *Cement and Concrete Composites*, vol. 47, pp. 69–74, 2014. DOI: 10.1016/j.cemconcomp.2013.05.004.

[8] C. Andrade, C. Alonso, and F. J. Molina, "Cover cracking as a funcion of bar corrosion: Part I - Experimental test," *Materials and Structures*, vol. 26, pp. 453–464, 1993. DOI: 10.1007/BF02472805.

[9] J. G. Cabrera, "Deterioration of concrete due to reinforcement steel corrosion," *Cement and Concrete Composites*, vol. 18, pp. 47–59, 1996. DOI: 10.1016/0958-9465(95)00043-7.

[10] C. Alonso, C. Andrade, J. Rodriguez, and J. M. Diez, "Factors controlling cracking of concrete affected by reinforcement corrosion," *Materials and Structures*, vol. 31, pp. 435–441, 1998. DOI: 10.1007/bf02480466.

[11] Y. Zhao, J. Yu, B. Hu, and W. Jin, "Crack shape and rust distribution in corrosion-induced cracking concrete," *Corrosion Science*, vol. 55, pp. 385–393, 2012. DOI: 10.1016/j.corsci.2011.11.002.

[12] C. Andrade, A. Cesetti, G. Mancini, and F. Tondolo, "Estimating corrosion attack in reinforced concrete by means of crack opening," *Structural Concrete*, vol. 17, no. 4, pp. 533–540, 2016. DOI: 10.1002/suco.201500114.

[13] M. Tahershamsi, I. Fernandez, K. Lundgren, and K. Zandi, "Investigating correlations between crack width, corrosion level and anchorage capacity," *Structure and Infrastructure Engineering*, vol. 13, no. 10, pp. 1294–1307, 2017. DOI: 10.1080/15732479.2016.1263673.

[14] F. U. A. Shaikh, "Effect of Cracking on Corrosion of Steel in Concrete," *International journal of Concrete Structures and Materials*, vol. 12, 2018. DOI: 10.1186/s40069-018-0234-y.

[15] E. Chen, C. G. Berrocal, I. Löfgren, and K. Lundgren, "Correlation between concrete cracks and corrosion characteristics of steel reinforcement in pre-cracked plain and fibre-reinforced concrete beams," *Materials and Structures*, vol. 53, 2020. DOI: 10.1617/s11527-020-01466-z.

[16] C. G. Berrocal, I. Fernandez, and R. Rempling, "The interplay between corrosion and cracks in reinforced concrete beams with non-uniform reinforcement corrosion," *Materials and Structures*, vol. 55, 2022. DOI: 10.1617/s11527-022-01956-2.

[17] Y. Zhao, A. Karimi, H. Wong, B. Hu, N. Buenfeld, and W. Jin, "Comparison of uniform and non-uniform corrosion induced damage in reinforced concrete based on a Gaussian description of the corrosion layer," *Corrosion Science*, vol. 53, pp. 2803–2814, 2011. DOI: 10.1016/j.corsci.2011.05.017.

[18] U. Angst and B. Elsener, "The size effect in corrosion greatly influences the prediction life span of concrete infrastructure," *Science Advances*, vol. 3, no. 8, 2017. DOI: 10.1126/sciadv.1700751.

[19] S. Rasheeduzzafar, S. Al-Saadoun, and S. Al-Gahtani, "Corrosion Cracking in Relation to Bar Diameter," *Journal of Materials in Civil Engineering*, vol. 4, no. 4, pp. 327–342, 1992. DOI: 10.1061/(ASCE)0899-1561(1992)4:4(327).

[20] H. Bui and K. Tan, "Multi-peak nonuniform model of rust distribution and corrosion-induced concrete cracking in reinforced concrete slabs," *Cement and Concrete Composites*, vol. 140, 2023. DOI: 10.1016/j.cemconcomp.2023.105087.

[21] Hansson, C.M., "Comments on electrochemical measurements of the rate of corrosion of steel in concrete," *Cement and Concrete Research*, vol. 14, no. 4, pp. 574–584, 1984. DOI: 10.1016/0008-8846(84)90135-2.

[22] Raupach, M., "Investigations on the influence of oxygen on corrosion of steel in concrete - Part 1," *Materials and Structures*, vol. 29, pp. 174–184, 1996. DOI: 10.1007/BF02486163.

[23] M. Pourbaix and Staehle, R.W., "Electrochemical Equilibria," in *Lectures on Electrochemical Corrosion*, N. Y. Springer, Ed., 1973. DOI: 10.1007/978-1-4684-1806-4_4.

[24] U. Angst, B. Elsener, Larsen, C.K., and Ø. Vennesland, "Critical chloride content in reinforced concrete - A review," *Cement and Concrete Research*, vol. 39, no. 12, pp. 1122–1138, 2009. DOI: 10.1016/j.cemconres.2009.08.006.

[25] Y. Zhou, B. Gencturk, ASCE, A.M., K. William, F. ASCE, and A. Attar, "Carbonation-Induced and Chloride-Induced Corrosion in Reinforced Concrete Structures," *Journal of Materials in Civil Engineering*, vol. 27, no. 9, 2014. DOI: 10.1061/(ASCE)MT.1943-5533.0001209.

[26] Tuutti, K., *Corrosion of steel in concrete*. PhD thesis. Stockholm, Sweden.: Swedish Cement and Concrete Research Institute, 1982.

[27] Parrott, L.J., "Damage caused by carbonation of reinforced concrete," *Materials and Structures*, vol. 23, pp. 230–234, 1990. DOI: 10.1007/BF02473023.

[28] A. Costa and J. Appleton, "Chloride penetration into concrete in marine environment - Part II: Predicting long term chloride penetration," *Materials and Structures*, vol. 32, pp. 354–359, 1999. DOI: 10.1007/BF02479627.

[29] Angst, U.M., "Predicting the time to corrosion initiation in reinforced concrete structures exposed to chlorides," *Cement and Concrete Research*, vol. 115, pp. 559–567, 2019. DOI: 10.1016/j.cemconres.2018.08.007.

[30] Y. Cao, C. Gehlen, U. Angst, L. Wang, Z. Wang, and Y. Yao, "Critical chloride content in reinforced concrete - An updated review considering Chinese experience," *Cement and Concrete Research*, vol. 117, pp. 58–68, 2019. DOI: 10.1017/j.cemconres.2018.11.020.

[31] R. Rodrigues, S. Gaboreau, J. Gance, I. Ignatiadis, and S. Betelu, "Reinforced concrete structures: A review of corrosion mechanisms and advances in electrical methods for corrosion monitoring," *Construction and Building Materials*, vol. 269, 2021. DOI: 10.1016/j.conbuildmat.2020.121240.

[32] S. Hong, S. Qin, P. Dong, *et al.*, "Quantification of rust penetration profile in reinforced concrete deducted by inverse modeling," *Cement and Concrete Composites*, vol. 111, 2020. DOI: 10.1016/j.cemconcomp.2020.103622.

[33] Taheri-Shakin, J. and A. Al-Mayah, "4D evolutions of cracks, voids, and corrosion products in reinforced concrete materials," *Scientific Reports*, vol. 13, 2023. DOI: 10.1038/s41598-023-48058-9.

[34] W. Feng, A. Tarakbay, Memon, S.A., W. Tang, and H. Cui, "Methods of accelerating chloride-induced corrosion in steel-reinforced concrete: A comparative review," *Construction and Building Materials*, vol. 289, 2021. DOI: 10.1016/j.conbuildmat.2021.123165.

[35] Y. Yuan, Y. Ji, and Shah, S.P., "Comparison of two accelerated corrosion techniques for concrete structures," *ACI Structural Journal*, vol. 104, pp. 344–347, 2007.

[36] J. Shi, J. Ming, and W. Sun, "Accelerated Corrosion Behavior of Steel in Concrete Subjected to Sustained Flexural Loading Using Electrochemical Methods and X-Ray Comnputed Tomography," *Journal of Materials in Civil Engineering*, vol. 30, p. 7, 2018. DOI: 10.1061/(ASCE)MT.1943-5533.0002337.

[37] C. Andrade, A. Alonso, and J. Sarría, "Corrosion rate evolution in concrete structures exposed to the atmosphere," *Cement and Concrete Composites*, vol. 24, pp. 55–64, 2002. DOI: 10.1016/S0958-9465(01)00026-9.

[38] S. Hong, G. Shi, F. Zheng, M. Liu, D. Hou, and B. Dong, "Characterization of the corrosion profiles of reinforcement with different impressed current densities by X-ray micro-computed tomography," *Cement and Concrete Composites*, vol. 109, 2020. DOI: 10.1016/j.cemconcomp.2020.103583.

[39] H. Jin, L. Zhang, B. Wang, C. Fang, and L. Wang, "Effects of electrode materials and potential gradient on electro-osmotic consolidation for marine clayey soils," *Frontiers in Earth Science*, vol. 12, 2024. DOI: 10.3389/feart.2024.1260045.

[40] El Maaddawy, T.A. and Soudki, K.A., "Effectiveness of Impressed Current Techniques to Simulation Corrosion of Steel Reinforcement in Concrete," *Journal of Materials in Civil Engineering*, vol. 15, no. 1, pp. 41–47, 2003. DOI: 10.1061/(ASCE)0899-1561(2003)15:1(41).

[41] H. Ye, C. Fu, N. Jin, and X. Jin, "Performance of reinforced concrete beams corroded under sustained service loads: A comparative study of two accelerated corrosion techniques," *Construction and Building Materials*, vol. 162, pp. 286–297, 2018. DOI: 10.1016/j.conbuildmat.2017.10.108.

[42] J. Rodriguez, Ortega, L.M., and Garcia, A.M., "Assessment of Structural Elements with Corroded Rebars," *Corrosion and corrosion protection of steel in concrete*, vol. 1, 1994.

[43] K. Lundgren, "Effect of corrosion on the bond between steel and concrete: an overview," *Magazine of Concrete Research*, vol. 59, no. 6, pp. 447–461, 2007. DOI: 10.1680/macr.2007.59.6.447.

[44] Van Steen, C., E. Verstrynge, M. Wevers, and L. Vandewalle, "Assessing the bond behaviour of corroded smooth and ribbed rebars with acoustic emission monitoring," *Cement and Concrete Research*, vol. 120, pp. 176–186, 2019. DOI: 10.1016/j.cemconres.2019.03.023.

[45] S. Robuschi, J. Sumearll, I. Fernandez, and K. Lundgren, "Bond of naturally corroded, plain reinforcing bars in concrete," *Structure and Infrastructure Engineering*, vol. 17, no. 6, pp. 792–808, 2021. DOI: 10.1080/15732479.2020.1768273.

[46] I. Sæther, "Bond deterioration of corroded steel bars in concrete," *Structure and Infrastructure Engineering*, vol. 7, no. 6, pp. 415–429, 2011. DOI: 10.1080/15732470802674836.

[47] Y. Zhao, X. Xu, Y. Wang, and J. Dong, "Characteristics of pitting corrosion in an existing reinforced concrete beam subjected to marine environment," *Construction and Building Materials*, vol. 234, 2020. DOI: 10.1016/j.conbuildmat.2019.117392.

[48] Apostolopoulos, C.A. and Papadopoulos, M.P., "Tensile and low cycle fatigue behavior of corroded reinforcing steel bars S400," *Construction and Building Materials*, vol. 21, no. 4, pp. 855–864, 2007. DOI: 10.1016/j.conbuildmat.2005.12.012.

[49] L. Song and Z. Yu, "Fatigue performance of corroded reinforced concrete beams strengthened with CFRP sheets," *Construction and Building Materials*, vol. 90, pp. 99–109, 2015. DOI: 10.1016/j.conbuildmat.2015.05.024.

[50] Du, Y.G., Clark, L.A., and Chan, A.H.C, "Effect of corrosion on ductility of reinforcing bars," *Magazine of Concrete Research*, vol. 57, no. 7, pp. 407–419, 2005. DOI: 10.1680/macr.2005.57.7.407.

[51] E. Chen, Berrocal, C.G., I. Löfgren, and K. Lundgren, "Corrosion Pattern and Mechanical Behaviour of Corroded Rebars in Cracked Plain and Fibre Reinforced Concrete," in *Fibre Reinforced Concrete: Improvements and Innovations*, 2021, pp. 477–488. DOI: 10.1007/978-3-030-58482-5_44.

[52] J. Cairns, Plizzari, G.A., Y. Du, Law, D.W., and C. Franzoni, "Mechanical properties of corrosion-damaged reinforcement," *ACI Materials Structures*, vol. 102, no. 4, pp. 256–264, 2005.

[53] EN 1992-1-1:2005, "Eurocode 2: Design of concrete structures - Part 1-1: General rules and rules for buildings," *Comité Européen de Normalisation (CEN). Europe.*, 2005.

[54] P. Pfändler, K. Bodie, G. Crotta, R. Siegwart, and U. Angst, "Non-destructive corrosion inspection of reinforced concrete structures using an autonomous flying robot," *Automation in Construction*, vol. 158, 2024. DOI: 10.1016/j.autcon.2023.105241.

[55] A. Menga, T. Kanstad, D. Cantero, L. Bathen, K. Hornbostel, and A. Klausen, "Corrosion-induced damages and failures of posttensioned bridges: A literature review," *Structural Concrete*, vol. 24, no. 1, pp. 84–99, 2022. DOI: 10.1002/suco.202200297.

[56] C. Andrade and C. Alonso, "Corrosion rate monitoring in the laboratory and on-site," *Construction and Building Materials*, vol. 10, no. 5, 1996. DOI: 10.1016/0950-0618(95)00044-5.

[57] C. Andrade and C. Alonso, "Test methods for on-site corrosion rate measurement of steel reinforcement in concrete by means of the polarization method," *Materials and Structures*, vol. 37, pp. 623–643, 2004. DOI: 10.1007/BF02483292.

[58] B. Elsener, C. Andrade, J. Gulikers, R. Polder, and M. Raupach, "Half-cell potential measurements – Potential mapping on reinforced concrete structures," *Materials and Structures*, vol. 36, pp. 461–471, 2003. DOI: 10.1007/BF02481526.

[59] W. Yodsudjai and T. Pattarakittam, "Factors influencing half-cell potential measurement and its relationship with corrosion level," *Measurement*, vol. 104, 2017. DOI: 10.1016/j.measurement.2017.03.027.

[60] E. Verstrynge, Van Steen, C., E. Vandecruys, and M. Wevers, "Steel corrosion damage monitoring in reinforced concrete structures with the acoustic emission technique: A review," *Construction and Building Materials*, vol. 349, 2022. DOI: 10.1016/j.conbuildmat.2022.128732.

[61] S. Yuyama, K. Yokoyama, K. Niitani, M. Ohtsu, and T. Uomoto, "Detection and evaluation of failures in high-strength tendon of prestressed concrete bridges by acoustic emission," *Construction and Building Materials*, vol. 21, pp. 491–500, 2007. DOI: 10.1016/j.conbuildmat.2006.04.010.

[62] Y. Kawasaki, T. Wakuda, T. Kobarai, and M. Ohtsu, "Corrosion mechanisms in reinforced concrete by acoustic emission," *Construction and Building Materials*, vol. 48, pp. 1240–1247, 2013. DOI: 10.1016/j.conbuildmat.2013.02.020.

[63] Van Steen, C., L. Pahlavan, M. Wevers, and E. Verstrynge, "Localisation and characterisation of corrosion damage in reinforced concrete by means of acoustic emission and X-ray computed tomography," *Construction and Building Materials*, vol. 197, pp. 21–29, 2019. DOI: 10.1016/j.conbuildmat.2018.11.159.

[64] A. Behnia, Chai, H.K., and T. Shiotani, "Advanced structural health monitoring of concrete structures with the aid of acoustic emission," *Construction and Building Materials*, vol. 65, pp. 282–302, 2014. DOI: 10.1016/j.conbuildmat.2014.04.103.

[65] Bažant, Z.P., "Physical Model for Steel Corrosion in Reinforced Sea Structures – Application," *Journal of the Structural Division*, vol. 105, no. 6, 1979. DOI: 10.1061/JSDEAG.0005169.

[66] Y. Liu and Weyers, R.E., "Modeling the Time-to-Corrosion Cracking in Chloride Contaminated Reinforced Concrete Structures," *ACI Materials Journals*, vol. 95, no. 6, pp. 675–680, 1998. DOI: 10.14359/410.

[67] L. Chernin, Val, D.V., and Volokh, K.Y., "Analytical modelling of concrete cover cracking caused by corrosion of reinforcement," *Materials and Structures*, vol. 43, pp. 543–556, 2010. DOI: 10.1617/s11527-009-9510-2.

[68] K. Lundgren, "Bond between ribbed bars and concrete. Part 2: The effect of corrosion," *Magazine of Concrete Research*, vol. 57, no. 7, pp. 383–395, 2005. DOI: 10.1680/macr.2005.57.7.383.

[69] J. Ožbolt, F. Oršanić, G. Balabanić, and M. Kušter, "Modeling damage in concrete caused by corrosion of reinforcement: coupled 3D FE model," *International Journal of Fracture*, vol. 178, pp. 233–244, 2012. DOI: 10.1007/s10704-012-9774-3.

[70] Van Steen, C., Van Beirendonck, T., R. Vrijdaghs, Hendriks, M.A.N., and E. Verstrynge, "A two-phased modelling approach for corrosion-induced concrete cracking and bond deterioration in reinforced concrete," *Engineering Structures*, vol. 294, 2023. DOI: 10.1016/j.engstruct.2023.116624.

[71] C. Andrade, F. Tavares, L. Toro, and J. Fullea, "Observations on the Morphology of Oxide Formation due to Reinforcement Corrosion," in *Modelling of Corroding Concrete Structures*, C. Andrade and J. Gulikers, Eds., 2011, pp. 179–193. DOI: 10.1007/978-94-007-0677-4_12.

[72] Wong, H.S., Angst U.M., Geiker, M.R., *et al.*, "Methods for characterising the steel-concrete interface to enhance understanding of reinforcement corrosion: a critical review by RILEM TC 262-SCI," *Materials and Structures*, vol. 55, no. 124, 2022. DOI: 10.1617/s11527-022-01961-5.

[73] Y. Zhao, H. Dai, H. Ren, and W. Jin, "Experimental study of the modulus of steel corrosion in a concrete port," *Corrosion Science*, vol. 56, pp. 17–26, 2012. DOI: 10.1016/j.corsci.2011.11.004.

[74] A. Dehoux, F. Bouchelaghem, and Y. Berthaud, "Micromechanical and microstructural investigation of steel corrosion layers of variable age developed under impressed current method, atmospheric or saline conditions," *Corrosion Science*, vol. 97, pp. 49–61, 2015. DOI: 10.1016/j.corsci.2015.04.016.

[75] Fischer-Cripps, A.C., "Critical review of analysis and interpretation of nanoindentation test data," *Surface & Coating Technology*, vol. 200, pp. 4153–4165, 2006. DOI: 10.1016/j.surfcoat.2005.03.018.

[76] A. Ouglova, Y. Berthaud, M. François, and F. Foct, "Mechanical properties of an iron oxide formed by corrosion in reinforced concrete structures," *Corrosion Science*, vol. 48, pp. 3988–4000, 2006. DOI: 10.1016/j.corsci.2006.03.007.

[77] G. Xu, L. Liu, H. Bao, Q. Wang, and J. Zhao, "Mechanical properties of steel corrosion products in reinforced concrete," *Materials and Structures*, vol. 50, no. 115, 2017. DOI: 10.1617/s11527-016-0985-3.

[78] Solgaard, A.O.S., A. Michel, M. Geiker, and H. Stang, "Concrete cover cracking due to uniform reinforcement corrosion," *Materials and Structures*, vol. 46, pp. 1781–1799, 2013. DOI: 10.1617/s11527-013-0016-6.

[79] Jamali, A. and Angst, U. and Adey, B. and Elsener, B., "Modeling of corrosion-induced concrete cover cracking: A critical analysis," *Construction and Building Materials*, vol. 42, pp. 225–237, 2013. DOI: 10.1016/j.conbuildmat.2013.01.019.

[80] A. Neville, *Properties of Concrete*, 5th ed. Harlow, England: Pearson Education Limited, 2011, ISBN: 978-0-273-75580-7.

[81] A. Michel, Pease, B.J., Geiker, M.R., H. Stang, and Olesen, J.F., "Monitoring reinforcement corrosion and corrosion-induced cracking using non-destructive x-ray attenuation measurements," *Cement and Concrete Research*, vol. 41, pp. 1085–1094, 2011. DOI: 10.1016/j.cemconres.2011.06.006.

[82] I. Petre-Lazar, "Aging assessment of concrete structures (in french)," Ph.D. dissertation, Laval University, Quebec, Canada, 2000.

[83] Wong, H.S., Zhao, Y.X., Karimi, A.R., Buenfeld, N.R., and Jin, W.L., "On the penetration of corrosion products from reinforcing steel into concrete due to chloride-induced corrosion," *Corrosion Science*, vol. 52, pp. 2469–2480, 2010. DOI: 10.1016/j.corsci.2010.03.025.

[84] M. Beck, J. Goebbels, and A. Burkert, "Application of X-ray tomography for the verification of corrosion processes in chloride contaminated mortar," *Materials and Corrosion*, vol. 58, no. 3, pp. 207–210, 2007. DOI: 10.1002/maco.200604049.

[85] B. Šavija, M. Luković, Hosseini, S.A.S., J. Pacheco, and E. Schlangen, "Corrosion induced cover cracking studied by X-ray computed tomography, nanoindentation, and energy dispersive X-ray spectrometry (EDS)," *Materials and Structures*, vol. 48, pp. 2043–2062, 2015. DOI: 10.1617/s11527-014-0292-9.

[86] P. Zhang, Z. Liu, Y. Wang, J. Yang, S. Han, and T. Zhao, "3D neutron tomography of steel reinforcement corrosion in cement-based composites," *Construction and Building Materials*, vol. 162, pp. 561–565, 2018. DOI: 10.1016/j.conbuildmat.2017.12.057.

[87] E. Rossi, R. Polder, O. Copuroglu, T. Nijland, and B. Šavija, "The influence of defects at the steel/concrete interface for chloride-induced pitting corrosion of naturally-deteriorated 20-years-old specimens studied through X-ray Computed Tomography," *Construction and Building Materials*, vol. 235, 2020. DOI: 10.1016/j.conbuildmat.2019.117474.

[88] Angst, U.E., E. Rossi, Käthler, C.B., *et al.*, "Chloride-induced corrosion of steel in concrete – insights from bimodal neutron and X-ray microtomography combined with ex-situ microscopy," *Materials and Structures*, vol. 57, no. 56, 2024. DOI: 10.1617/s11527-024-02337-7.

[89] S. Robuschi, A. Tengattini, J. Dijkstra, I. Fernandez, and K. Lundgren, "A closer look at corrosion of steel reinforcement bars in concrete using 3D neutron and X-ray computed tomography," *Cement and Concrete Research*, vol. 144, 2021. DOI: 10.1016/j.cemconres.2021.106439.

[90] M. A., Pease, B.J., A. Peterová, Geiker, M.R., H. Stang, and Thybo, A.E.A., "Penetration of corrosion products and corrosion-induced cracking in reinforced cementitious materials: Experimental investigations and numerical simulations," *Cement and Concrete Composites*, vol. 47, pp. 75–86, 2014. DOI: 10.1016/j.cemconcomp.2013.04.011.

[91] A. Tengattini, N. Lenoir, E. Andò, and G. Viggiani, "Neutron imaging for geomechanics: A review," *Geomechanics for Energy and the Environment*, vol. 27, 2021. DOI: 10.1016/j.gete.2020.100206.

[92] V. Cnudde and M. Boone, "High-resolution X-ray computed tomography in geosciences: A review of the current technology and applications," *Earth-Science Reviews*, vol. 123, pp. 1–17, 2013. DOI: 10.1016/j.earscirev.2013.04.003.

[93] S. Brisard, M. Serdar, and P. Monteiro, "Multiscale X-ray tomography of cementitious materials: A review," *Cement and Concrete Research*, vol. 128, 2020. DOI: 10.1016/j.cemconres.2019.105824.

[94] N. Kardjilov, I. Manke, A. Hilger, M. Strobl, and J. Banhart, "Neutron imaging in materials science," *Materials today*, vol. 14, pp. 248–256, 2014. DOI: 10.1016/S1369-7021(11)70139-0.

[95] L. Feldkamp, L. Davis, and J. Kress, "Practical cone-beam algorithm," *Journal of the Optical Society of America A*, vol. 1, pp. 612–619, 1984. DOI: 10.1364/JOSAA.1.000612.

[96] C. Jacobsen, "Relaxation of the Crowther criterion in multislice tomography," *Optics Letters*, vol. 43, no. 18, 10.1364/OL.43.004811, 2018.

[97] Crowther, R.A., DeRosier, D.T., and A. Klug, "The Reconstruction of a Three-Dimensional Structure from Projections and its Application to Electron Microscopy," *Proceedings of the Royal Society of London. Series A, Mathematical and Physical Science*, vol. 317, no. 1530, pp. 319–340, 1970.

[98] K. Naresh, K. Khan, R. Umer, and W. Cantwell, "The use of X-ray computed tomography for design and process modeling of aerospace composities: A review," *Materials & Design*, vol. 190, 2020. DOI: 10.1016/j.matdes.2020.108553.

[99] J. Kastner and C. Heinzl, "X-Ray Tomography," in *Handbook of Advanced Nondestructive Evaluation*, Springer Nature Switzerland, 2019, pp. 1095–1166. DOI: 10.1007/978-3-319-26553-7.

[100] A. Tengattini, N. Lenoir, E. Andò, *et al.*, "NeXT-Grenoble, the Neutron and X-ray tomograph in Grenoble," *Nuclear Instruments and Methods in Physics Research Section A: Accelerators, Spectrometers, Detectors and Associated Equipment*, vol. 968, 2020. DOI: 10.1016/j.nima.2020.163939.

[101] Meganck, J.A., Kozloff, K.M., Thornton, M.M., Broski, S.M., and Goldstein, S.A., "Beam hardening artifacts in micro-computed tomography scanning can be reduced by X-ray beam filtration and the resulting images can be used to accurately measure BMD," *Bone*, vol. 45, pp. 1104–1116, 2009. DOI: 10.1016/j.bone.2009.07.078.

[102] O. Stamati, E. Roubin, E. Andò, and Y. Malecot, "Phase segmentation of concrete x-ray tomographic images at meso-scale: Validation with neutron tomogrpahy," *Cement and Concrete Composites*, vol. 88, pp. 8–16, 2018. DOI: 10.1016/j.cemconcomp.2017.12.011.

[103] E. Maire and P. Withers, "Quantitative X-ray tomography," *International Materials Review*, vol. 59, 2014. DOI: 10.1179/1743280413Y.0000000023.

[104] F. Maes, A. Collignon, D. Vandermeulen, G. Marchal, and P. Suetens, "Multimodality Image Registration by Maximization of Mutual Information," *IEEE Transactions on Medical Imaging*, vol. 16, pp. 187–198, 1997. DOI: 10.1109/42.563664.

[105] E. Tudisco, C. Jailin, A. Mendoza, *et al.*, "An extension of digital volume correlation for multimodality image registration," *Measurement Science and Technology*, vol. 28, 2017. DOI: 10.1088/1361-6501/aa7b48.

[106] E. Roubin, E. Andò, and S. Roux, "The colours of concrete as seen by X-rays and neutrons," *Cement and Concrete Composites*, vol. 104, 2019. DOI: 10.1016/j.cemconcomp.2019.103336.

[107] M. Sutton, J.-J. Orteu, and H. Schreier, *Image Correlation for Shape, Motion and Deformation Measurements: Basic Concepts, Theory and Applications*. Springer, New York, USA, 2009. DOI: 10.1007/978-0-387-78747-3.

[108] F. Hild and S. Roux, "Comparison of Local and Global Approaches to Digital Image Correlation," *Experimental Mechanics*, vol. 52, pp. 1503–1519, 2012. DOI: 10.1007/s11340-012-9603-7.

[109] B. Wang and B. Pan, "Subset-based local vs. finite element-based global digital image correlation: A comparison study," *Theoretical & Applied Mechanics Letters*, vol. 6, pp. 200–208, 2016. DOI: 10.1016/j.taml.2016.08.003.

[110] J. Poissant and F. Barthelat, "A Novel "Subset Splitting" Procedure for Digital Image Correlation on Discontinious Displacement Fields," *Experimental Mechanics*, vol. 50, pp. 353–364, 2010. DOI: 10.1007/s11340-009-9220-2.

[111] T. Becker, "Extracting fracture properties from digital image and volume correlation displacement data: A review," *Strain*, vol. 60, no. 4, 2024. DOI: 10.1111/str.12469.

[112] O. Stamati, E. Andò, E. Roubin, *et al.*, "spam: Software for Practical Analysis of Materials," *The Journal of Open Source Software*, vol. 5, no. 51, 2020. DOI: 10.21105/joss.02286.

[113] G. Lu and D. Wong, "An adaptive inverse-distance weighting spatial interpolation technique," *Computers & Geosciences*, vol. 34, no. 9, pp. 1044–1055, 2008. DOI: 10.1016/j.cageo.2007.07.010.

[114] A. Alhede and Van Steen, C., "Measuring Corrosion-Induced Deformations in Reinforced Concrete: An Image-Based Approach by Means of X-ray Computed Tomography.," in Barros, J.A.O., Cunha, V.M.C.F., Sousa, H.S., Matos, J.C., Sena-Cruz, J.M. (eds) 4th fib International Conference on Concrete Sustainability (ICCS2024). ICCS 2024. *Lecture Notes in Civil Engineering,* vol 574. Springer, Cham., 2024. DOI: 10.1007/978-3-031-80724-4_2.

[115] G. Mancini and F. Tondolo, "Effect of bond degradation due to corrosion - a literature study," *Structural Concrete*, vol. 15, pp. 408–418, 2014. DOI: 10.1002/suco.201300009.

[116] Luna Inc, *High-Definition Fiber Optic Strain Sensors*, Last accessed 2023-03-06, 2023. [Online]. Available: https://lunainc.com/product/hd6s.

[117] Luna Inc, *Optical Distributed Sensor Interrogator*, Last accessed 2022-11-21, 2022. [Online]. Available: https://lunainc.com/product/odisi-6000-series.

[118] L. Chang, K. Frid, R. Kruse, R. Jänicke, and K. Lundgren, "Dual-scale study of pre-damage, water boundary conditions and frost interaction in concrete," *Materials and Structures*, vol. 58, no. 74, 2025. DOI: 10.1617/s11527-025-02599-9.

[119] H. Sun, C. Jiang, K. Cao, *et al.*, "Monitoring of steel corrosion and cracking in cement paste exposed to combined sulfate-chloride attack with X-ray microtomography," *Construction and Building Materials*, vol. 302, 2021. DOI: 10.1016/j.conbuildmat/2021.124345.

[120] K. Suda, S. Misra, and K. Motohashi, "Corrosion products of reinforcing bars embedded in concrete," *Corrosion Science*, vol. 35, no. 5–8, pp. 1543–1549, 1993. DOI: 10.1016/0010-938X(93)90382-Q.

[121] Daniel, E.F., C. Li, C. Wang, *et al.*, "Insights into the characteristics of corrosion products formed on the contact and exposed regions of C1045 steel bolt and nut fasteners exposed to aqueous chloride environments," *Journal of Materials Science & Technology*, vol. 135, pp. 250–264, 2023. DOI: 10.1016/j.jmst.2022.06.037.

[122] Nam, J-G., Hartt, W.H., and K. Kim, "Effects of Air Void at the Steel-Concrete Interface on the Corrosion Initiation of Reinforcing Steel in Concrete under Chloride Exposure," *Journal of the Korea Concrete Institute*, vol. 17, no. 5, pp. 829–834, 2005.

[123] C. Wen, Y. Tian, Z. Mai, J. Hu, and G. Wang, "Effect of macropores at the steel-concrete interface on localized corrosion behaviour of steel corrosion," *Cement and Concrete Composites*, vol. 129, 2022. DOI: 10.1016/j.cemconcomp.2022.104510.

[124] Angst, U.E., Geiker, M.R., Alonso, M.C., *et al.*, "The effect of the steel-concrete interface on chloride-induced corrosion initiation in concrete: a critical review by RILEM TC 262-SCI," *Materials and Structures*, vol. 52, no. 88, 2019. DOI: 10.1617/s11527-019-1387-0.

[125] D. Dauti, A. Tengattini, Dal Pont, S., N. Toropovs, M. Briffaut, and B. Weber, "Analysis of moisture migration in concrete at high temperature through in-situ neutron tomography," *Cement and Concrete Research*, vol. 111, pp. 41–55, 2018. DOI: 10.1016/j.cemconres.2018.06.010.

[126] A. Nemati, B. Lukić, A. Tengattini, R. Gupta, M. Briffaut, and P. Séchet, "Rapid in situ neutron tomography and X-ray imaging of vapour condensation in fractured sandstone," *Transport in Porous Media*, vol. 150, 2023. DOI: 10.1007/s11242-023-02014-3.

[127] DIANA FEA BV, *DIANA Finite Element Analysis – Theory Manual, Release 10.7*, D. Ferreira, Ed. Delft, The Netherlands: DIANA FEA BV, 2024.

[128] H. Reinhardt, H. Cornelissen, and Hordijk, D.A., "Tensile tests and failure analysis of concrete," *Journal of Structural Engineering*, vol. 112, no. 11, pp. 2462–2477, 1986. DOI: 10.1061/(ASCE)0733-9445(1986)112:11(2462).

[129] Hordijk, D.A, "Local approach to fatigue of concrete," Ph.D. dissertation, Delft University of Technology, 1991.

[130] G. Markeset and A. Hillerborg, "Softening of concrete in compression - loalization and size effects," *Cement and Concrete Research*, vol. 25, no. 4, pp. 702–708, 1995. DOI: 10.1016/0008-8846(95)00059-L.

[131] Walsh, C.L., P. Tafforeau, Wagner, W.L., *et al.*, "Imaging intact human organs with local resolution of cellular structures using hierarchical phase-contrast tomography," *Nature Methods*, vol. 18, pp. 1532–1541, 2021. DOI: 10.1038/s41592-021-01317-x.